J. Fluid Mech. (2013), *vol.* 725, *pp.* 117–151.
doi:10.1017/jfm.2013.191

Inertial and barotropic instabilities of a free current in three-dimensional rotating flow

G. F. Carnevale[1],†, R. C. Kloosterziel[2] and P. Orlandi[3]

[1]Scripps Institution of Oceanography, University of California, San Diego, La Jolla, CA 92093, USA

[2]School of Ocean and Earth Science and Technology, University of Hawaii, Honolulu, HI 96822, USA

[3]Dipartimento di Meccanica e Aeronautica, University of Rome, 'La Sapienza', via Eudossiana 18, 00184 Roma, Italy

(Received 23 August 2012; revised 30 January 2013; accepted 9 April 2013)

A current in a homogeneous rotating fluid is subject to simultaneous inertial and barotropic instabilities. Inertial instability causes rapid mixing of streamwise absolute linear momentum and alters the vertically averaged velocity profile of the current. The resulting profile can be predicted by a construction based on absolute-momentum conservation. The alteration of the mean velocity profile strongly affects how barotropic instability will subsequently change the flow. If a current with a symmetric distribution of cyclonic and anticyclonic vorticity undergoes only barotropic instability, the result will be cyclones and anticyclones of the same shape and amplitude. Inertial instability breaks this symmetry. The combined effect of inertial and barotropic instability produces anticyclones that are broader and weaker than the cyclones. A two-step scheme for predicting the result of the combined inertial and barotropic instabilities is proposed and tested. This scheme uses the construction for the redistribution of streamwise absolute linear momentum to predict the mean current that results from inertial instability and then uses this equilibrated current as the initial condition for a two-dimensional simulation that predicts the result of the subsequent barotropic instability. Predictions are made for the evolution of a Gaussian jet and are compared with three-dimensional simulations for a range of Rossby numbers. It is demonstrated that the actual redistribution of absolute momentum in the three-dimensional simulations is well predicted by the construction used here. Predictions are also made for the final number and size of vortices that result from the combined inertial and barotropic instabilities.

Key words: geophysical and geological flows, instability, turbulent flows

1. Introduction

In a recent study of the turbulent breakdown and equilibration of unstable vortices in rotating homogeneous flow, we demonstrated that it is possible to accurately predict the outcome of the full three-dimensional evolution using only inertial instability theory and two-dimensional simulations of barotropic flow (Carnevale *et al.* 2011). For a barotropic vortex in a homogeneous flow, the primary instabilities are inertial

† Email address for correspondence: gcarnevale@ucsd.edu

and barotropic. Early in the evolution of the unstable vortex, it undergoes an inertial instability that causes the coherent vortex to degenerate into three-dimensional turbulent flow. This turbulent phase is followed by a relatively slower two-dimensional phase dominated by barotropic instability (Kloosterziel & van Heijst 1991; Orlandi & Carnevale 1999). The final result is a number of interacting cyclones and anticyclones. For the unstable vortex, predictions based on absolute angular momentum mixing were able to correctly capture the number of vortices that resulted from the breakup of the original vortex as well as the distribution of vorticity within these vortices. The method of prediction is a two-step scheme. The first step uses inertial instability theory based on mixing of angular momentum (Kloosterziel, Carnevale & Orlandi 2007*a*) to predict the equilibrated flow that would result if barotropic instability did not occur. The second step uses two-dimensional simulation to predict the outcome of barotropic instability acting on the equilibrated flow given by the first step. This two-step prediction scheme is justified when the inertial instability is faster than the barotropic instability, and the larger the difference in the growth rates of the two instabilities, the more successful the prediction. Encouraged by our results for predicting the evolution of unstable vortices, we turn here to the question of whether a similar scheme for predicting the evolution of unstable, initially barotropic, currents in three-dimensional rotating flow can be successful. Kloosterziel, Orlandi & Carnevale (2007*b*) provide the groundwork for making such a scheme. They showed how an absolute-momentum mixing argument can be used to predict the equilibration of inertial instability acting alone on unstable planar flows in streamwise-uniform flow. Here we demonstrate that the predicted redistribution of absolute momentum, which is also referred to as 'geostrophic momentum', is also achieved in fully three-dimensional flow. Then we show how this result can be combined with two-dimensional simulations of barotropic instability to provide a prediction for the combined effect of inertial and barotropic instabilities in fully three-dimensional flow.

This work has potential applications for both the atmosphere and the oceans. Although baroclinic instability is an important ingredient in understanding evolution of atmospheric and oceanic currents in general, under certain conditions, inertial and barotropic instabilities are known to dominate. This is the case in the atmosphere for stably stratified flows in tropical regions where the effect of rotation is not so strongly felt as at middle latitudes (Winter & Schmitz 1998). For the oceans, it has been suggested that the occurrence of numerous intense cyclones of 10–25 km scale, called 'spiral eddies', is due to inertial instability of currents in the upper mixed layer (Shen & Evans 2002). In most locations these eddies are cyclonic (Munk *et al.* 2000), although observations off the Norwegian coast suggest that there $\sim$15 % of the spiral eddies are anticyclonic and that their diameters tend to be larger than that of their cyclonic counterparts (Eldevik & Dysthe 2002). Although Munk *et al.* (2000) and Eldevik & Dysthe (2002) argue that baroclinic instability is a strong candidate for the source of these spiral eddies, it is possible that they can be created in the unstratified mixed layer. Indeed, Shen & Evans (2002) showed that no stratification is needed to produce spiral eddies and provided three-dimensional simulations that capture the formation of spiral eddies in a homogeneous flow. Furthermore, Shen & Evans (1998) found that in numerical simulations the inertial instability has a growth rate about twice that of the barotropic instability, which suggests that the two-step prediction scheme that we used in Carnevale *et al.* (2011) for unstable vortices should also work in the case of unstable currents that produce spiral eddies.

The coordinate system that we shall use is shown in figure 1. The system is in uniform rotation around the z-axis with angular rotation rate $f/2$, where f is

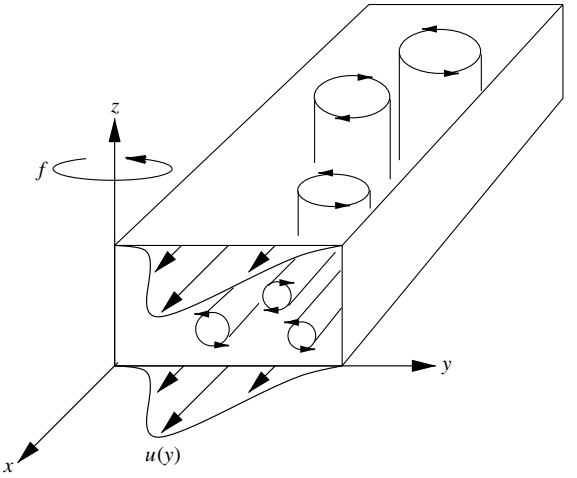

FIGURE 1. Schematic of the rotating channel showing a barotropic flow $u(y)$ and the vorticity produced by two types of instabilities (inertial and barotropic). The Coriolis parameter f is twice the angular velocity of the rotating system. Here it is assumed to be invariant in space and time. Horizontal vortex tubes (aligned along the x-axis) represent pure inertial instability, and vertical vortex tubes (aligned along the z-axis) represent pure barotropic horizontal-shear instability.

the Coriolis parameter, which is taken here to be invariant in space and time. The velocities in the x, y and z directions are u, v and w and the components of vorticity are ω_x, ω_y and ω_z. A streamwise-uniform barotropic jet takes the form $u = u(y)$, $v = 0$ and $w = 0$. Of the three components of vorticity, only $\omega_z = -\mathrm{d}u/\mathrm{d}y$ is non-zero. Such a jet is indicated by the arrows pointing in the x direction in figure 1. The absolute or geostrophic momentum of this jet is $m(y) = u(y) - fy$. The term 'absolute momentum' is sometimes also used for $u(y) - (f/2)y$, which would be the momentum measured in an inertial frame (see Markowski & Richardson 2010, for a discussion of this point). The absolute or potential vorticity is $q = \omega_z + f$. This jet will be inertially unstable if at any point $fm(y)$ increases with increasing y (Charney 1973; Holton 1979). The inertial instability transfers energy from the jet into vortical motion oriented in the streamwise direction, that is into the ω_x field. The vortices thus created are illustrated as rolls parallel to the x-axis in figure 1. Since the basic flow is a jet and thus has inflection points (i.e. points where $\mathrm{d}^2u/\mathrm{d}y^2$ vanishes), the flow satisfies Rayleigh's necessary condition for barotropic instability (Holton 1979). The barotropic instability produces a meandering of the jet that leads to the formation of vortices oriented along the z-axis as illustrated by the vertical rolls in figure 1. Thus, in the three-dimensional flow, the evolution will generally be complicated involving the production of both ω_x and ω_z through linear instability and ω_y through nonlinear effects. As in the case of the inertial instability of vortices (see, for example, Kloosterziel & van Heijst 1991), the inertial instability phase of the evolution tends to be turbulent with vertical velocities reaching, if not exceeding, that of the maximum velocity in the basic state. Subsequently, the flow tends to two-dimensionalize under the continued influence of ambient rotation. In this phase, barotropic instability dominates. In the end, we are left with a number of strong cyclonic vortices and somewhat broader and weaker (in amplitude) anticyclones or even just a diffuse background of anticyclonic vorticity.

In what follows, we first review the predictions for equilibration of inertial instability in § 2. Then, the effect that inertial-instability equilibration has on the fastest growing barotropic instability modes is examined in § 3. Fully three-dimensional simulations of the combined inertial and barotropic instability are presented in § 4. There it is shown that the momentum mixing construction for redistribution of absolute momentum works very well for predicting the evolution of the vertically and streamwise averaged profile of velocity during the early evolution of the three-dimensional flow. In § 5, predictions are made for the combined effect of inertial and barotropic instabilities and are compared to the results of the three-dimensional simulations. The comparison shows that our two-step prediction scheme is able to capture the variation with Rossby number of the mean number of vortices produced and the asymmetry in the magnitudes of the amplitudes of the cyclones and anticyclones. The results are summarized in § 6.

2. Nonlinear evolution in streamwise-uniform inertial instability

We focus on a Gaussian jet as a model of a free barotropic current. The streamwise velocity of the basic state is

$$U(y) = U_0 \exp(-y^2/\ell^2) \tag{2.1}$$

with absolute momentum $m = M(y) = U(y) - fy$. This basic flow has only vertical relative vorticity $\omega_z = \Omega(y) = -\mathrm{d}U/\mathrm{d}y$. In terms of the vorticity, $f\,\mathrm{d}M/\mathrm{d}y = -f(\Omega + f)$. Thus, inertial instability will occur for anticyclonic vorticity larger in magnitude than $|f|$. In terms of the potential vorticity of the basic flow, $Q \equiv \Omega + f$, the instability occurs for values of y such that $fQ < 0$ or $f\,\mathrm{d}M/\mathrm{d}y > 0$.

For simplicity, we will take $f > 0$ and scale all lengths by ℓ and time by the advective time scale $T = \ell/U_0$. Without loss of generality we take $U_0 > 0$. In these units, the basic flow is $U(y) = \exp(-y^2)$. We define the Rossby number of the flow as $Ro \equiv U_0/f\ell$ and the Reynolds number as $Re = U_0\ell/\nu$. Thus,

$$M(y) = U(y) - \frac{y}{Ro}, \tag{2.2}$$

and

$$\frac{\mathrm{d}M}{\mathrm{d}y} = \frac{\mathrm{d}U}{\mathrm{d}y} - \frac{1}{Ro} = -(\Omega(y) + Ro^{-1}). \tag{2.3}$$

The flow can only be inertially unstable for Ro such that $Q = \Omega(y) + Ro^{-1}$ is negative somewhere. This cannot occur if $Ro^{-1} > -\min_y \Omega$. Thus, $Ro_{cr} \equiv -\min_y \Omega$ defines a critical value such that for $Ro > Ro_{cr}$ there will be instability. For our model flow we have

$$\Omega(y) = -\mathrm{d}U/\mathrm{d}y = 2y\exp(-y^2) \tag{2.4}$$

and

$$\mathrm{d}\Omega/\mathrm{d}y = (2 - 4y^2)\exp(-y^2), \tag{2.5}$$

so that the minimum value of Ω occurs at $y = -1/\sqrt{2}$ with $\min_y \Omega = -\sqrt{2/\mathrm{e}} \approx -0.858$. Thus,

$$Ro_{cr} = \sqrt{\frac{\mathrm{e}}{2}} \approx 1.17. \tag{2.6}$$

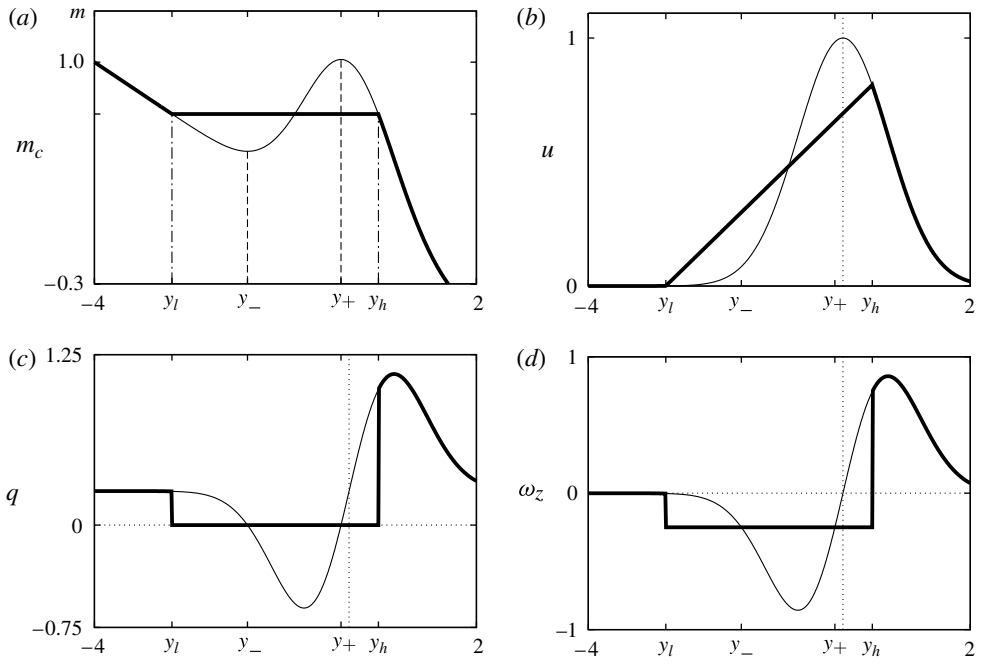

FIGURE 2. (*a*) A construction for predicting the extent of the equilibration range according to (2.8) which conserves total absolute momentum m (see the text). (*b*) The equilibrated velocity field. (*c*) The equilibrated potential vorticity $q = \omega_z + 1/Ro$. (*d*) The equilibrated vorticity ω_z. Here y_l and y_h are the limits on the equilibration range and y_- and y_+ are the limits on the linear instability range. Thin lines are the initial profiles based on the Gaussian current (2.1) for the case $Ro = 4$. The thick lines are the predicted inviscid equilibrated profiles. The thin vertical and horizontal dotted lines in (*b*), (*c*) and (*d*) are the zero axes.

Since the vorticity distribution in the Gaussian jet is antisymmetric about $y = 0$, the maximum and minimum values of the vorticity in the basic flow occur at $y = \pm 1/\sqrt{2}$ and $\max_y \omega_z = -\min_y \omega_z = 1/Ro_{cr} \approx 0.858$.

For $Ro > Ro_{cr}$ there will be a range of y of non-vanishing length for which $Q = \Omega + Ro^{-1}$ is negative. This defines the linear instability region. The endpoints of this region, where the absolute vorticity Q vanishes, are given by

$$\Omega(y) = 2y\mathrm{e}^{-y^2} = -\frac{1}{Ro}. \tag{2.7}$$

There are only two solutions to (2.7), both of which are negative and so lie in the region of negative vorticity. We denote these solutions as y_- and y_+ with $y_- < y_+$. In the limit of $Ro \to \infty$ we have $y_- = -\infty$ and $y_+ = 0$. Figure 2(*a*) shows the graph of $M(y)$ (thin line) along with the positions of y_- and y_+ for the case of $Ro = 4$, a case that we will examine in some detail.

2.1. *Predicted equilibrium from pure inertial instability*

Inertial instability begins in the region bounded by y_- and y_+ and acts to redistribute absolute angular momentum in such a way as to create a new velocity profile such that $\mathrm{d}m/\mathrm{d}y$ is no longer positive anywhere or, equivalently, that $q \geqslant 0$ everywhere. In other words, the evolution drives the flow to a new, inertially stable state. There are

many ways to change m to accomplish this even while conserving the total absolute momentum.

In Kloosterziel *et al.* (2007*b*), we demonstrated that at high Reynolds number the equilibrated profile approximates the $Re = \infty$ prediction based on a simple mathematical construction that conserves total absolute momentum. This construction is illustrated in figure 2(*a*). The predicted equilibrated $m(y)$ is drawn as a thick curve (which covers $M(y)$ where they coincide at high and low values of y). Note that $M(y) \sim -y/Ro$ for $|y| \to \infty$. In figure 2(*a*), we see that in our construction the absolute momentum has been redistributed in such a way that the deficit of momentum $(m_c - M(y))$ from the range of y surrounding y_- is filled with excess momentum from the range surrounding y_+. This is done in such a way that the total absolute momentum is unchanged. The value of m_c and the limits of the mixing range y_l and y_h are defined by solving the conservation condition:

$$\int_{y_l}^{y_h} (M(y) - m_c)\,\mathrm{d}y = 0. \tag{2.8}$$

To solve this equation in practice, we first choose a value of m_c. Solving $M(y) = m_c$ defines tentative values of y_l and y_h. The value of the integral in (2.8) is tested, and depending on its sign, a new guess is made for m_c that is correspondingly higher or lower than the original choice. The process is iterated in an efficient manner to quickly converge to the value that makes the integral vanish (to within some preassigned tolerance).

Note from figure 2 that the predicted equilibration range may extend far beyond the inertial instability range. In particular, note that the values of y_h may be positive. Although the linear instability regime $[y_-, y_+]$ is always confined to negative values of y where initially $\omega_z < 0$ and $q = (\omega_z + 1/Ro_{cr}) < 0$ (see figure 2*c*,*d*), mixing can extend into the region $y > 0$ where initially there was only cyclonic vorticity $\omega_z > 0$.

The predicted final equilibrated $m(y)$ is given by

$$\begin{aligned} m(y) &= m_c \qquad \text{for } y \in [y_l, y_h] \\ &= M(y) \qquad \text{for } y \notin [y_l, y_h]. \end{aligned} \tag{2.9}$$

From this equilibrated momentum $m(y)$, we can construct the equilibrated velocity profile $u(y)$. This is shown in figure 2(*b*). Note that the original symmetry of the Gaussian jet has been lost. This will have important consequences on the types of vortices produced by the meandering of the jet, as will be seen below.

Figure 2(*c*) shows the potential vorticity q of the basic state and the equilibrated vorticity. Note that the basic state has $q < 0$ for $y \in (y_-, y_+)$. Equilibration to an inertially stable state clearly requires an adjustment so that $q \geqslant 0$ everywhere, but that alone does not determine the range over which the profile will be changed. That range is determined uniquely by our construction, which demands that q be reduced to zero between y_l and y_h.

Figure 2(*d*) shows the relative vertical vorticity ω_z of the basic state and the equilibrated state. These are the same as the corresponding absolute vorticity graphs save for a shift in amplitude by $1/Ro$ (=1/4 in this case). Originally, in the Gaussian jet, ω_z was antisymmetric about $y = 0$. As noted above, the maximum and minimum values of the vorticity in the Gaussian jet are $\max_y \omega_z = -\min_y \omega_z = Ro_{cr}^{-1} \approx 0.858$. In the equilibrated state, the minimum vorticity becomes $-1/Ro$, which can be much smaller in magnitude than the maximum vorticity depending on the value of Ro.

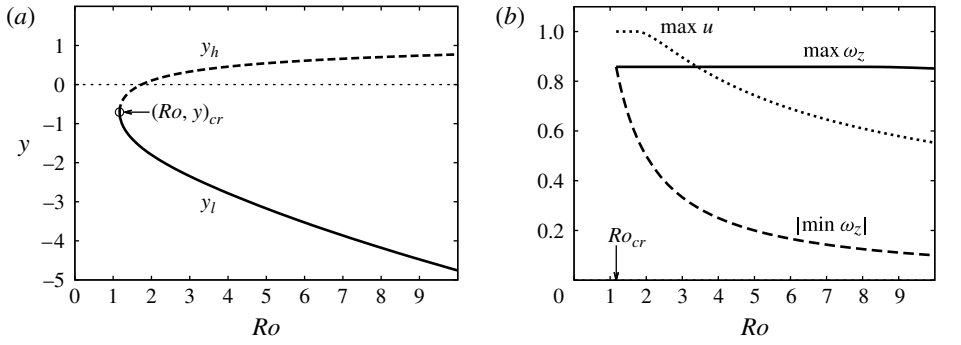

FIGURE 3. (*a*) The predicted limits of the inertial instability equilibration range, y_l and y_h as functions of Ro. (*b*) The predicted $\max_y \omega_z$ (solid), $|\min \omega_z| = 1/Ro$ (long dash) and $\max u = \Gamma_+/L_x$ (short dash) as a functions of Ro.

2.2. *Asymmetry of the equilibrium vorticity distribution*

Since barotropic instability cannot change vorticity amplitudes, the asymmetry in vorticity introduced by the inertial instability will prove crucial in determining the types of vortices that emerge from the combined instabilities in fully three-dimensional evolution of the jet. It is important to understand how the profile of equilibrated ω_z changes with increasing Ro. The range of positive and negative vorticity and their peak values are determined by y_l and y_h.

In figure 3(*a*), we show how the limits on the equilibration region $[y_l, y_h]$ vary with Ro. Note that although both y_l and y_h are negative for $Ro \approx Ro_{cr}$, y_h is positive for $Ro \gtrapprox 1.75$. As $Ro \to \infty$, we have $y_l \to -\infty$ and $y_h \to +\infty$. The range where $\omega_z = -1/Ro$ (i.e. where $q = 0$) for the predicted equilibrium is given by $y \in (y_l, y_h)$. This range grows monotonically with Ro for $Ro > Ro_{cr}$. The region of positive vorticity only changes when Ro is sufficiently large so that $y_h > 0$. The range of positive vorticity is $(0, \infty)$ for $Ro \lessapprox 1.75$. For $Ro \gtrapprox 1.75$, the range of positive vorticity decreases as (y_h, ∞) with increasing Ro.

The graphs of $\max_y \omega_z$ and $|\min_y \omega_z|$ are shown in figure 3(*b*). The maximum value of the positive vorticity remains nearly constant over the full range of Ro shown. In contrast, $\min_y \omega_z = -1/Ro$ changes rapidly as Ro increases. The behaviour of $\max_y \omega_z$ can be deduced from figure 2(*d*). As Ro increases, $\max_y \omega_z$ remains constant until y_h reaches $y = 1/\sqrt{2}$ where the basic state has its peak vorticity. This occurs for $Ro \approx 8.23$. Although it is not obvious from figure 3(*b*), beyond this value of Ro, $\max_y \omega_z$ decreases monotonically with Ro.

Even though the vorticity distribution becomes very asymmetric with increasing Ro, the total positive vorticity remains equal to the magnitude of the total negative vorticity. This follows from the condition that u vanishes for $|y| \to \infty$ and that the flow is uniform in x. These conditions require that the total circulation vanish. In a domain of arbitrarily length L_x in the x direction, the magnitude of the total positive circulation Γ_+ must be just the negative of the total negative circulation Γ_-, with these defined by

$$\Gamma_\pm = \int_0^{L_x} \mathrm{d}x \int_{-\infty}^{+\infty} \omega_z \theta(\pm\omega_z)\, \mathrm{d}y, \tag{2.10}$$

where θ is the Heaviside step function. Since in the equilibrated flow $\omega_z = -\mathrm{d}u/\mathrm{d}y$, Γ_+/L_x is equivalent to $\max_y u$ as can be seen by integrating ω_z from the beginning of the range of positive vorticity, where $u(y) = \max_y u$, to $y = \infty$. The behaviour of $\max_y u$ as a function of Ro can be understood from figure 2(*b*). As long as $y_h < 0$, $\max_y u = U(y = 0) = 1$. With $Ro \gtrapprox 1.75$, $y_h > 0$ and hence $\max_y u = U(y_h)$. The behaviour of $\max_y u$ is shown in figure 3(*b*). Note that, even though the peak velocity in the equilibrated current decreases with increasing Ro (for $Ro \gtrapprox 1.75$), the net flow $\int u\,\mathrm{d}y$ is independent of Ro. This follows from the fact that our construction for calculating the equilibrated flow does not change the total absolute momentum of the flow and, hence, cannot change the net flow, which for all Ro has the value $\sqrt{\pi}$.

2.3. *Numerical simulation of pure inertial instability*

The redistribution of absolute momentum in inertial instability is accomplished by the streamwise vortices that are created by the instability. In order to make a direct comparison between how this mixing works in the streamwise invariant flow and the fully three-dimensional flow, we examine here the evolution of the flow for the case $Ro = 4$ with a simulation that allows no variation in the streamwise direction. The comparison to the fully three-dimensional case will be made in § 4. In the streamwise invariant simulation, we see the effects of inertial instability alone since there can be no barotropic instability. In the vertical (z) direction, the boundary conditions are periodic, and in the spanwise (y) direction there are free-slip boundaries. The initial state is taken as the basic Gaussian jet plus a perturbation $u'(y, z)$ added at each grid point. Here u' is a random number generated from a uniform distribution with root mean square (r.m.s.) value 10^{-4}. There is no flow initially in the y or z directions, thus the ω_x field is initially zero. The instability begins with the creation of streamwise vortices with ω_x of alternating sign stacked in the vertical z direction. The vortices are found within the initial instability region as shown in figure 4(*a*). They create overturning motions typically associated with inertial instability. They grow in strength and develop nonlinear interactions with their neighbours. On the side near y_-, each positive vortex pairs with the negative vortex just above it, forming a dipolar head that propagates in the negative y direction. On the side near y_+, each positive vortex pairs with the negative vortex below it, forming a dipolar head that propagates in the positive y direction. In this way, the disturbance caused by the instability moves out of the initial instability region (see figure 4*b*). The distance that the disturbance spreads is mostly limited to the range $[y_l, y_h]$ as defined by our construction (see figure 4*c*). Some dipole heads do go beyond the limits prescribed by our construction, but they then weaken and tend to turn around and sometimes return to the predicted mixing region (see figure 4*d*). The net effect of the dipoles that escape from the predicted limits is small, as we shall see in the next figure, and that effect diminishes with increasing Reynolds number as shown in Kloosterziel *et al.* (2007*a*,*b*).

During this evolution, the action of the streamwise vortices is to mix the absolute momentum $m = u - y/Ro$ laterally, changing the profile of the vertically averaged m according to our construction. Figure 5(*a*) shows how the vertically averaged profile of absolute momentum $\overline{m}(y)$ changes with time. From $t = 0$ until about $t = 40$ the profile changes little. In that period, there is just slow decay due to viscous dissipation. Around $t = 45$ there is a rapid evolution in which the local high and low of $\overline{m}$ are equalized resulting, by $t = 60$, in a profile that approximates the constant m_c predicted by our construction. After this there is again just slow viscous dissipation. The evolution of the vertically averaged velocity field is shown in figure 5(*b*). There is

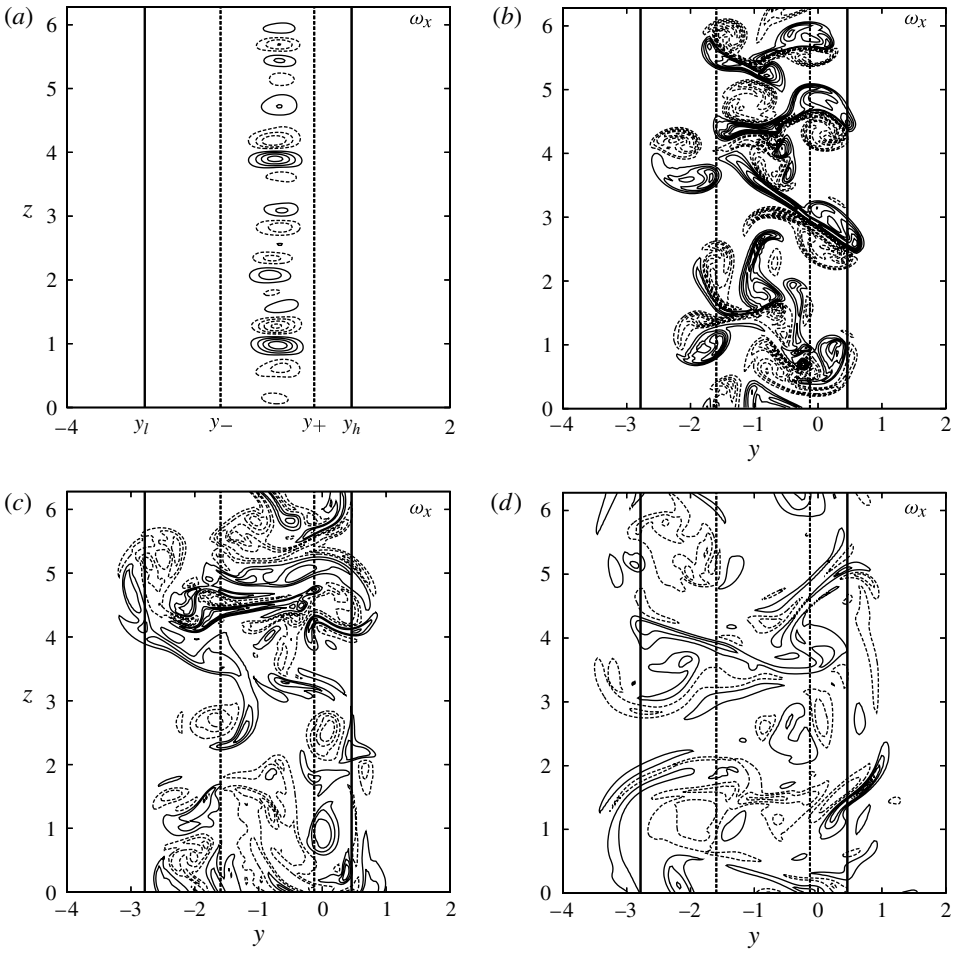

FIGURE 4. Contour plots of ω_x from an x-independent simulation with $Ro = 4$ and $Re = 2500$ at times (*a*) $t = 30$, (*b*) 45, (*c*) 60 and (*d*) 75. The initial instability region, where $Q < 0$ or $\mathrm{d}M/\mathrm{d}y > 0$, is bounded by the vertical thin dashed lines, at y_- and y_+. The predicted limits of the inertial instability equilibration range, y_l and y_h, are indicated by the thin vertical solid lines. Only a portion of the full computational domain $y \in [-5, 5]$ and $z \in [0, 4\pi]$ is shown. The resolution for this simulation was 256×512 gridpoints. Positive/negative contour values are represented by solid/dashed curves. The zero contour level is not drawn. The contour level increment in (*a*) is $\Delta\omega_x = 0.1$, and in (*b–d*) is $\Delta\omega_x = 0.5$.

a rapid collapse of $\overline{u}$ onto the linear profile in the equilibration range, just as predicted by our construction. After this there is just slow viscous decay.

2.4. *Wavenumber and growth rate of the fastest growing mode*

As discussed in the introduction, the ability to predict the outcome of the three-dimensional evolution of the jet in rotating flow will depend on the ability to separate the effects of inertial and barotropic instabilities. This will be possible when the inertial instability occurs on a shorter time scale than that of the barotropic instability. Thus, quantitative information about the growth rates of both instabilities is relevant. The important quantity for our purposes at this point is the growth rate of the

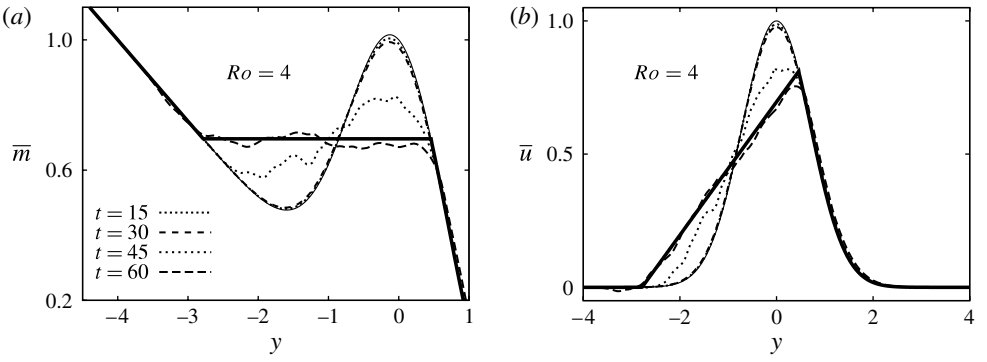

FIGURE 5. The evolution of the vertically averaged streamwise velocity u and absolute momentum m from an x-independent simulation with $Ro = 4$ and $Re = 2500$. (a) The vertically averaged m at four times along with the unperturbed initial profile (thin solid curve) and the predicted equilibrated profile (thick solid curve). (b) The vertically averaged u at the same times as shown in (a). The dashed patterns are the same as defined in the key of (a).

fastest growing mode of the inertial instability for given Ro and Re. This can be obtained by standard methods for solving the linearized stability eigenvalue problem for perturbations about the basic flow $u = U(y)$, assuming no variation in x, the streamwise direction. The details on how to solve for the eigenmode that has the greatest growth rate γ_{max} are given in the appendix.

The vertical wavenumber k_z of the fastest growing mode obtained by solving the eigenvalue problem is shown as a function of Re and Ro in figure 6(a) (thick solid and dashed curves). The curve for $Ro = 2$ lies above that for $Ro = 4$, and both curves show that k_z increases monotonically with Re. The variation of k_z with Re, at least for large Re, can be obtained analytically by asymptotic methods as shown in Kloosterziel & Carnevale (2008, Appendix B by S. Griffiths). In our non-dimensional formulation, the result to leading order is

$$k_z \sim 2^{-1/2} Ro_{cr}^{-1/6} Ro^{-1/6} Re^{1/3}. \tag{2.11}$$

Thus, k_z scales with $Re^{1/3}$ for large Re. This scaling was also found in the inertial instability of barotropic vortices (Kloosterziel *et al.* 2007*a*). Formula (2.11) is graphed as a thin dashed line for $Ro = 2$ and a thin solid line for $Ro = 4$ in figure 6(a). Comparison of the thick and thin lines show that they converge well for $Re \gtrsim 2 \times 10^4$. Formula (2.11) also shows that for fixed Re, k_z decreases with increasing Ro as verified by the comparison of the results for $Ro = 2$ and $Ro = 4$ shown in figure 6(a). This figure also includes the results of estimating k_z of the fastest growing mode from direct numerical simulations. A small amplitude perturbation with a given vertical wavenumber is prescribed initially, and then the subsequent exponential growth of its amplitude is measured. By varying the vertical wavenumber of the initial perturbation, an estimate can be made for the wavenumber of the fastest growing mode. The results are shown as open circles ○ for $Ro = 2$ and open squares □ for $Ro = 4$, and they show reasonable agreement with the theoretical predictions.

The growth rate for the fastest growing mode as a function of Ro and Re is shown in figure 6(b). The thick solid curve is the theoretical result for maximum growth rate for $Re \to \infty$, in which limit the maximum growth rate is achieved in the limit $k_z \to \infty$.

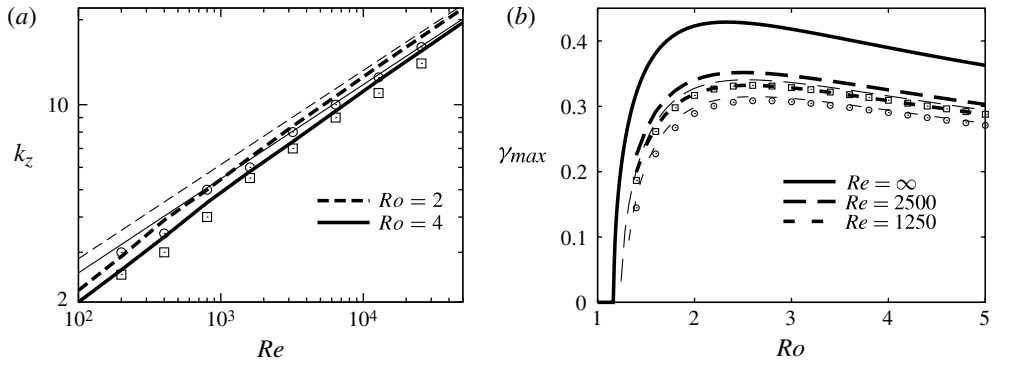

FIGURE 6. (*a*) The most unstable wavenumber k_z as a function of Re for $Ro = 2$ and 4. The thick lines are the results from solving the eigenvalue problem as discussed in the appendix. The thin lines (dashed and solid) are the asymptotic large Re predictions according to (2.11). Results from simulations on a grid of 129×129 on the domain $(y, z) \in [-10, 10] \times [0, 4\pi]$ are shown as points: $Ro = 2$ (○) and $Ro = 4$ (□). (*b*) Inertial instability growth rates. The thick solid line represents the theoretical growth rate for $Re = \infty$ according to (2.12) or equivalently (2.14). The thick dashed lines are the results for $Re = 2500$ and $Re = 1250$ from the eigenvalue calculation discussed in the appendix. The thin dashed lines represent the corresponding approximations according to (2.13). Results from simulations on a grid of 129×129 points covering the domain $y \in [-10, 10]$ and $z \in [0, 4\pi]$ are shown as points: (□) $Re = 2500$; (○) $Re = 1250$.

Analytically, in the inviscid limit, we have

$$\gamma_{max} = \sqrt{-\min_y Ro^{-1} Q}, \tag{2.12}$$

or, in the more familiar dimensional form, $\gamma_{max} = \sqrt{-\min_y fQ}$ when $\min_y fQ < 0$. The thick dashed curves are the growth rates obtained by solving the eigenvalue problem as discussed in the appendix. Only results for $Re = 1250$ and $Re = 2500$ are shown since these are the Reynolds numbers relevant to our three-dimensional simulations, which are limited to relatively low Re due to constraints on resolution and computational time.

The asymptotic estimate for large Re for the square of the maximum growth rate γ_{max} is given by Kloosterziel & Carnevale (2008, Appendix B by S. Griffiths). In our non-dimensional units, the result to the first two leading orders is

$$\gamma_{max}^2 \sim Ro^{-2} Ro_{cr}(Ro - Ro_{cr}) - 3Re^{-1/3} Ro^{-4/3} Ro_{cr}^{-5/6} (Ro - Ro_{cr})^{1/2}. \tag{2.13}$$

In the limit $Re \to \infty$ this reduces to

$$\gamma_{max} \sim Ro^{-1} Ro_{cr}^{1/2} (Ro - Ro_{cr})^{1/2}. \tag{2.14}$$

Formulae (2.13) and (2.14) are valid when $Ro > Ro_{cr}$, that is when there is inertial instability. The inviscid limit (2.14) is equivalent to (2.12) given above.

Graphs of the asymptotic formula (2.13) for γ_{max} for $Re = 1250$ and $Re = 2500$ are drawn as thin dashed curves in figure 6(*b*). There is some quantitative difference when compared with the results of the eigenvalue problem, as should be expected since these values of Re are significantly lower than the value 2×10^4, above which we found good agreement between the asymptotic results and the eigenvalue analysis as shown in figure 6(*a*). The asymptotic result falls short of the eigenvalue problem

result at, for example, $Ro = 4$ by $\sim 4.5\,\%$ for $Re = 1250$, but only by about $3\,\%$ at the higher value $Re = 2500$. Streamwise-uniform numerical simulations of the inertial instability were performed to compare with the theoretical predictions. The resolution of these simulations was just sufficient to resolve the fastest growing modes of the linear instability. The growth rates from the numerical simulations are added as points: $\square$ for $Re = 2500$ and $\bigcirc$ for $Re = 1250$. The numerical simulation results fall short of the eigenvalue analysis, for example for $Re = 2500$ at $Ro = 2.6$, where the curves peak, by $\sim 6\,\%$. Among the possible sources of error for the growth rates in the numerical simulations is the fact that the values of the vertical wavenumber k_z are quantized for the finite height of the domain used in these simulations, making the result typically an underestimate if the fastest growing mode is not one of these quantized values. The resolution is another suspect source of error, but grid refinement tests indicate that the data points are accurate to better than $3\,\%$, so that the accuracy displayed here is sufficient for present purposes.

In the next section, we consider the barotropic instability of the Gaussian jet and its inertially equilibrated profile $U(y)$. Whereas the growing modes of pure inertial instability have the streamwise (along-flow) wavenumber $k_x = 0$ and vertical wavenumber $k_z \neq 0$, the growing modes of the barotropic instability have $k_z = 0$ and $k_x \neq 0$. These two types of instabilities are at opposite extremes of the possible fully three-dimensional instability: for inertial instability the perturbed flow remains invariant in the streamwise (x) direction (hence, the occasional use of the word 'symmetric instability' to describe inertial instability), while for barotropic instability the flow remains invariant in the vertical direction, which is perpendicular to the flow direction. Little can be said analytically about the stability of a parallel shear flow $U(y)$ when subjected to fully three-dimensional perturbations, that is, perturbations with both $k_x \neq 0$ and $k_z \neq 0$. But Griffiths (2008) showed analytically that, in a continuously rotating stratified fluid for large vertical wavenumbers k_z and small but non-zero streamwise wavenumbers k_x, the growth rate of the ensuing 'asymmetric inertial instability' is generally lower than for the pure inertial instability ($k_x = 0$). His conclusions were corroborated through numerical stability analysis. For circular flows (vortices) with or without stratification and rotation, Billant & Gallaire (2005) reached the same conclusion: the symmetric inertial instability at large vertical wavenumbers k_z has a larger growth rate than the asymmetric instability, the modes of which vary in the along-flow direction (perturbations with a non-zero azimuthal wavenumber). This was already observed in an earlier numerical study by Smyth & McWilliams (1998). Interestingly, Bouchut, Ribstein & Zeitlin (2011), who studied elements of inertial and asymmetric inertial instability of a jet in a two-layer model with a free surface, found that the asymmetric inertial instability can have higher growth rates than the (symmetric) inertial instability. Although there are signs of absolute momentum homogenization in their simulations, the essential character of inertial instability is absent: the overturning motions or streamwise vortices as seen in figure 4, for example, which lead to the momentum mixing or homogenization, cannot occur in such a model because it is layer-wise columnar. Also in their model, the symmetric instability is absent if the density ratio for the two layers is small, whereas in a continuously stratified fluid it will always occur when $\min_y fQ < 0$ provided the Reynolds number is large enough. Thus it seemed that for the homogeneous flow problem studied here we can suppose that the findings of Griffiths (2008) and Billant & Gallaire (2005) that the pure inertial instability will be faster than slightly asymmetric instability (small k_x) are more relevant. But it has come to our attention that in a recent study of the same jet considered by Bouchut *et al.* (2011) in a continuously stratified model it was again

found that slightly asymmetric instability is faster than symmetric instability (Ribstein, Plougonven & Zeitlin 2013, and private communication). How this can be reconciled with the predictions of Billant & Gallaire (2005) and Griffiths (2008) is not clear at the moment. Our interest here is focused on the question whether we can predict the outcome of the fully three-dimensional evolution if the perturbation growth rate at one extreme, i.e. pure inertial instability, exceeds the growth rate at the other extreme, i.e. pure barotropic instability (for either the original jet or predicted equilibrated jet).

3. Barotropic instability of the inertially equilibrated current

Next, we consider the barotropic instability of the inertially equilibrated current profile predicted by our construction in § 2. Barotropic flow in a homogeneous fluid is equivalent to pure two-dimensional flow. The equations of evolution of two-dimensional flow do not involve the Rossby number. However, dependence on Ro is introduced into the problem when we take the inertially equilibrated profile as the initial condition of the flow, because the form of that profile does depend on Ro. Thus, we can talk about how barotropic instability (after inertial equilibration) varies with Ro. We illustrate the main effects on barotropic instability of increasing Ro through a series of simulations in § 3.1. Then in § 3.2, we calculate the barotropic instability growth rates as a function of Ro.

3.1. *An example of how barotropic instability varies with Ro*

We wish to illustrate some of the most important effects that inertial equilibration of a current has upon the subsequent barotropic instability of the flow. We will present here three numerical simulations: one corresponding to $Ro < Ro_{cr}$, for which the Gaussian jet profile is unaltered by inertial instability, and two with $Ro > Ro_{cr}$, in which the initial velocity profiles are as we predicted in § 2 based on absolute linear momentum redistribution in the Gaussian jet. Some perturbation is needed to initiate the evolution in all of these cases because the basic profiles are independent of x, the streamwise coordinate, and are, hence, stationary even though unstable. In the three examples that we will examine, the basic profiles are given a perturbation that is sinusoidal in x. The simulations were performed on a horizontal computational grid of 256×512 points representing $x \in [0, 4\pi]$ by $y \in [-10, 10]$, with $Re = 2500$.

3.1.1. *Case $Ro < Ro_{cr}$: the Gaussian jet*

For $Ro < Ro_{cr}$ there is no inertial instability in the three-dimensional flow. Thus, our prediction from § 2 for such Ro is that the Gaussian profile is not altered. The perturbation that we use to initiate the flow can conveniently be written as a perturbation to the streamfunction:

$$\delta\psi = a\mathrm{e}^{-y^2}\sin(k_x x), \tag{3.1}$$

where a is the amplitude of the perturbation and k_x the wavenumber in the streamwise direction. An example of the evolution of the Gaussian jet subjected to this initial perturbation with $a = 10^{-4}$ and $k_x = 1$ is illustrated in the first column of figure 7. The sequence in time is from top to bottom (*a–d*). The initial perturbation gives a sinuous character to the initial flow, that is the extremes of positive and negative vorticity are out of phase considering their location in the streamwise direction. It turns out that the fastest growing barotropic mode is this sinuous mode. There is also a growing varicose (also called 'sausage') mode for the Gaussian profile, but this turns out to grow more

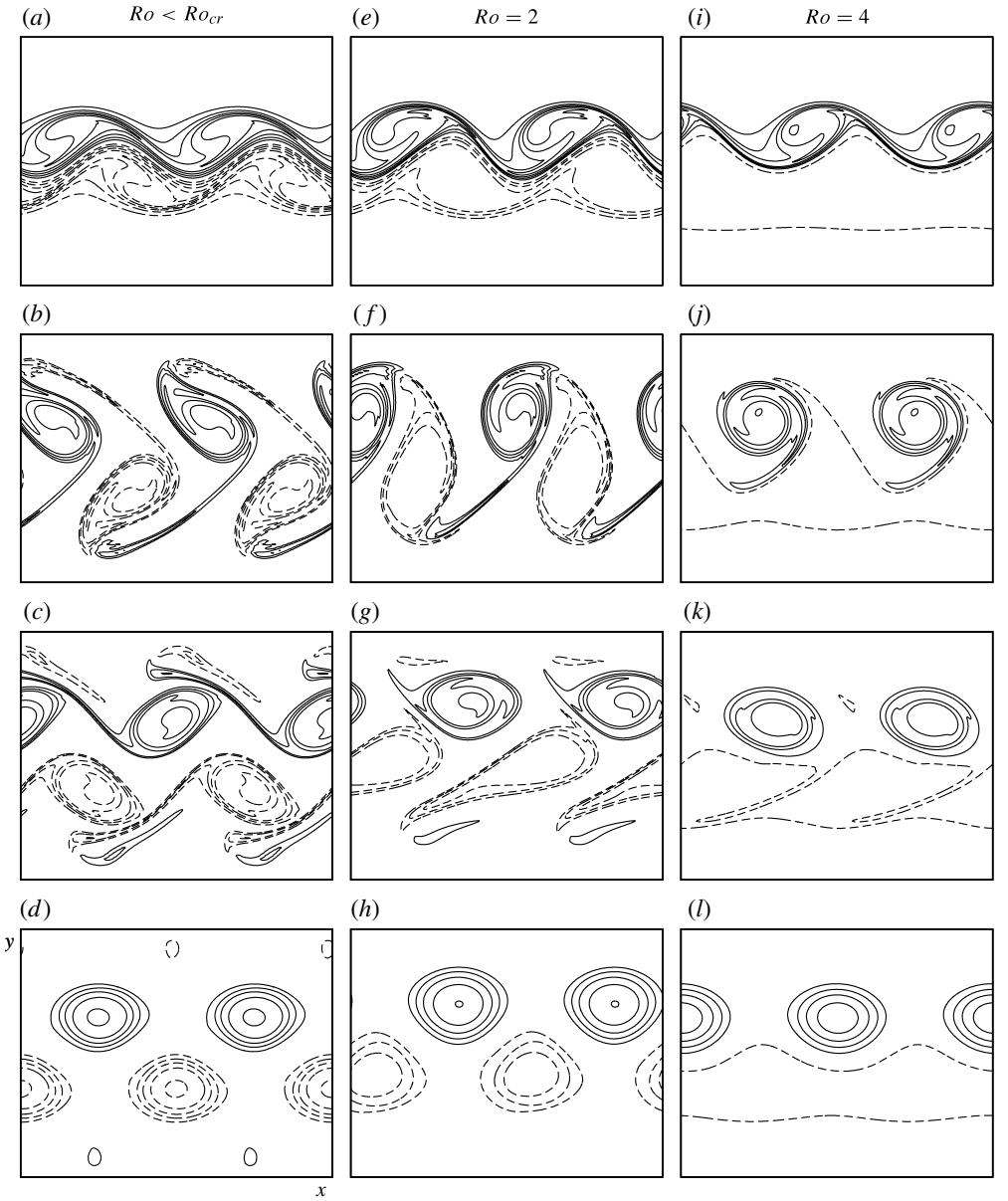

FIGURE 7. Contour plots of the evolving vorticity field ω_z from two-dimensional simulations with $Re = 2500$. Three cases are represented: $Ro < Ro_{cr}$ (first column), $Ro = 2$ (second column) and $Ro = 4$ (third column). The panels shown in each column correspond to increasing time: according to $Ro < Ro_{cr}$, (*a*) $t = 50$, (*b*) $t = 70$, (*c*) $t = 85$, (*d*) $t = 165$; according to $Ro = 2$, (*e*) $t = 65$, (*f*) $t = 80$, (*g*) $t = 95$, (*h*) $t = 200$; or according to $Ro = 4$: (*i*) $t = 65$, (*j*) $t = 80$, (*k*) $t = 105$, (*l*) $t = 200$. Solid/dashed lines correspond to positive/negative values of ω_z. The contour interval is 0.15 (the zero contour is not shown). The computational grid was 256×512 points representing $x \in [0, 4\pi]$ by $y \in [-10, 10]$. Although the full range is shown in the x-direction, only the part $y \in [-5, 5]$ in the y direction is displayed. For $Ro < Ro_{cr}$ the unperturbed current is the Gaussian jet. For $Ro = 2, 4$ the unperturbed flows are the inertially equilibrated currents. Barotropic instability was initiated with a perturbation (3.1) with $k_x = 1$ and amplitude $a = 10^{-4}$.

slowly than the sinuous mode, as discussed by Flierl, Malanotte-Rizzoli & Zabusky (1987). In the varicose mode the positions of the extremes of positive and negative vorticity are in phase.

In the final panel for this case, figure 7(*d*), we see that the evolution results in a vortex street where the vortices on each side of the 'street' are of opposite sign but of equal shape and strength. The initial extrema of the vorticity are given by $\omega_z = \pm Ro_{cr}^{-1} \approx 0.858$ as discussed in § 2. The final values would be unchanged from these in inviscid flow; however, here with $Re = 2500$, they are somewhat reduced in magnitude as a result of viscous dissipation. The important thing is that in figure 7(*d*) the magnitude of the maximum vorticity in the cyclones equals that in the anticyclones. This reflects the same symmetry as in the initial vorticity field. Figure 7(*d*) represents a long-term quasi-stationary state of the flow. In this simulation, this vortex street persisted until $t = 350$ after which it broke down when pairs of opposite-signed vortices formed dipoles that propagated away from the original jet axis.

3.1.2. *Case $Ro > Ro_{cr}$: the inertial-instability equilibrated jet*

For cases with $Ro > Ro_{cr}$, the equilibration by inertial instability breaks the symmetry of the initial condition. As shown in § 2, the magnitude of the amplitude of the anticyclonic vorticity in the equilibrated jet is less than that of the cyclonic jet (see figure 2 for the case $Ro = 4$). This leads to asymmetry in the barotropic instability. To illustrate how this affects the evolution of the jet, we performed simulations as just described above for the Gaussian jet, but here taking the basic profile to be that predicted by our absolute momentum mixing construction for the cases $Ro = 2$ and $Ro = 4$. We use exactly the same perturbation as was used in the Gaussian jet case, that is (3.1) with $a = 10^{-4}$ and $k_x = 1$.

Our numerical simulations cannot completely capture the effect of the discontinuities in the vertical vorticity field ω_z at $y = y_l$ and $y = y_h$ predicted by our construction (see figure 2*d*). In the vorticity evolution equation, the vorticity is differentiated with respect to y converting these step discontinuities into delta functions which cannot be properly represented in numerical simulations. In the two-dimensional simulations presented here, we have just calculated ω_z and its derivatives with finite differences on our discrete grid and ignored this problem. In a sense, this provides a one grid mesh space filter of the discontinuities. We have not seen any significant differences for the results when changing the resolution of the grid.

The evolution of ω_z in the case $Ro = 2$ is illustrated in the second column in figure 7. The initial minimum vorticity in this case is $-1/Ro = -0.5$, while the initial maximum vorticity is $1/Ro_{cr} \approx 0.858$ as explained in § 2. Because the growth rate of the instability is different for the two cases, $Ro < Ro_{cr}$ and $Ro = 2$, the times represented by the panels in the first two columns are not the same: they have been chosen to give a good representation of the phases of the evolution in each case. Comparing the panels in the second column for $Ro = 2$ with those in the first column for $Ro < Ro_{cr}$, we note the cyclone–anticyclone symmetry that we see in the first column is lost in the second column. By the time of the last figure 7(*h*), in the second column, the $Ro = 2$ column, we see that the major difference with the $Ro < Ro_{cr}$ case shown in figure 7(*d*) is the asymmetry of the vorticity distributions of the cyclones and anticyclones in the $Ro = 2$ case. In the anticyclones the vorticity distribution is 'flatter' than that in the cyclones, and the shape of the anticyclones is somewhat more 'angular' than that of the cyclones. Note that the low-amplitude, small, secondary vortices visible at the top and bottom of figure 7(*d*) for $Ro < Ro_{cr}$ have counterparts in

the $Ro = 2$ flow; however, their amplitudes are just too weak to be evident with this contour interval.

The $Ro = 4$ column in figure 7 contrasts very strongly with the symmetric Gaussian jet, the $Ro < Ro_{cr}$ case. For $Ro = 4$, the effect of the inertial instability equilibration has made the anticyclonic vorticity much weaker in amplitude and much more diffuse than the cyclonic vorticity. The initial amplitude of the anticyclonic vorticity is $-Ro^{-1} = -0.25$, while as we can see from figure 2(*d*), the initial peak cyclonic vorticity is the same as the peak vorticity in the Gaussian jet: $Ro_{cr}^{-1} \approx 0.858$. The very angular structure of the anticyclonic field in figure 7(*j*) results from the advection of the diffuse anticyclonic vorticity around the much more concentrated cyclonic vorticity. Although the total positive and negative circulations are identical, as discussed in § 2, this striking geometric effect is due to the contrast in the degree of localization of the positive and negative vorticity fields. This strong contrast persists into the quasi-steady state shown in figure 7(*l*).

In summary, inertial instability destroys the symmetry of the vorticity distribution of the Gaussian jet. For moderate, yet supercritical *Ro*, the subsequent barotropic instability results in cyclones that are of higher amplitude than the anticyclones. At sufficiently high *Ro*, the anticyclonic vorticity remains diffuse while the cyclonic vorticity still forms intense coherent vortices.

3.2. *Variation of barotropic instability growth rates with Ro*

If the growth rate for the barotropic instability is larger than that of the inertial instability, then the barotropic instability will compete strongly with the inertial instability and perhaps prevent the inertial instability from redistributing absolute momentum as in our construction. Thus, whether the evolution shown in figure 7 for either $Ro = 2$ or $Ro = 4$ is relevant to the evolution of the Gaussian jet in three-dimensional flow depends on whether the growth rate of the inertial instability is indeed higher than that for the barotropic instability.

We have calculated the barotropic instability growth rate for the Gaussian jet (our $Ro < Ro_{cr}$ case) as a function of zonal perturbation wavenumber k_x through consideration of perturbations of the form

$$\delta\psi = \mathrm{e}^{\mathrm{i}k_x(x-ct)}\phi(y). \tag{3.2}$$

The governing equation which follows from the inviscid two-dimensional vorticity equation is the Rayleigh instability equation (Drazin & Reid 1981):

$$(U-c)(\phi'' - k_x^2\phi) - U''\phi = 0 \tag{3.3}$$

where $U'' \equiv \mathrm{d}^2U/\mathrm{d}y^2$ (with $U(y)$ the Gaussian profile) and $\phi'' \equiv \mathrm{d}^2\phi/\mathrm{d}y^2$. The equation can be solved by writing $\phi(y)$ as a Fourier series of a finite number of terms, substituting this into the Rayleigh equation, and then solving the resulting matrix eigenvalue problem. Alternatively, one can skip the transformation to a Fourier series and simply evaluate (3.3) on a regular discrete grid of points. This second method also gives a matrix eigenvalue problem. We used both methods and found essentially the same results. The growth rates for the barotropic instability of the Gaussian are shown as the thick solid curve in figure 8. This curve represents the growth rate $\gamma = k_x \mathrm{Im}c$ (where Imc is the imaginary part of c) for the fastest growing mode of the Rayleigh equation as a function of k_x. Using a grid of 512 points, we find that the fastest growing mode occurs for $k_x \approx 0.9$. Alternatively, we used a Fourier cosine representation with 512 terms. These two calculations agree very well near the peak at

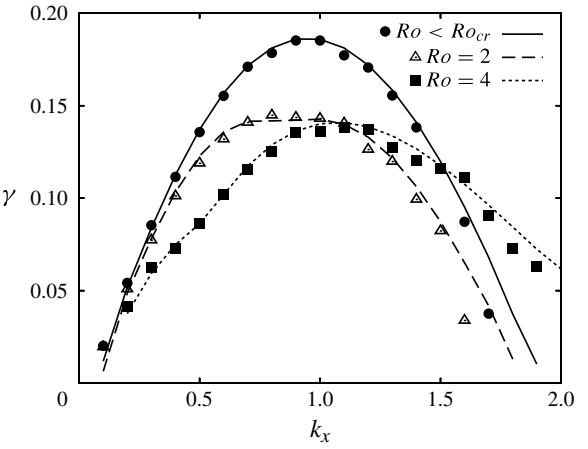

FIGURE 8. Barotropic growth rates as predicted (lines) from the Rayleigh equation (3.3) and as observed in inviscid two-dimensional simulations (symbols). The grid resolution was 512×512 gridpoints with $x \in [0, 2\pi/k_x]$ and $y \in [-5, 5]$. For $Ro < Ro_{cr}$, the basic profile is the Gaussian jet, while for $Ro = 2$ and $Ro = 4$ the basic profiles are those predicted by our momentum mixing construction given in § 2.

$k_x \approx 0.9$ with small differences occurring for much higher and smaller k_x. Using just 64 Fourier modes Flierl *et al.* (1987) found that the fastest growing mode occurred for $k_x \approx 0.8$, but otherwise the agreement with their result is very good over all.

As an additional check of our theoretical calculations of the growth rates, we also performed a series of inviscid simulations of the two-dimensional vorticity evolution equation in the x–y plane. Our two-dimensional numerical code is semi-conservative in energy and enstrophy, that is energy and enstrophy can be conserved to within a prescribed tolerance given a sufficiently small time step. Thus the code can be run inviscidly without numerical instability. The initial condition was taken as the Gaussian jet plus the sinusoidal perturbation (3.1). Theoretically, the amplitude of the perturbation could be chosen to be sufficiently small so that we could measure the growth of modes with a given k_x before nonlinear effects became significant. As a practical matter this can be difficult especially since there are growing modes of other wavenumbers that can compete with the mode that we are interested in. This problem can be avoided by linearizing the equations around the basic flow. As an alternative to explicit linearization, we achieved the same result by allowing only the growth of the single wavenumber of interest k_x. This was done by choosing the length of the computational domain in x to be $2\pi/k_x$, thus fitting only one complete wavelength of mode k_x and effectively filtering out all lower wavenumbers. Modes of wavenumber higher than k_x in the Fourier transform in the x-direction were eliminated by spectral truncation. The simulation then allowed only the growth of the k_x Fourier mode. The results from these simulations are shown in figure 8 as the filled circles, labelled $Ro < Ro_{cr}$ in the key, overlaying the corresponding solid curve from the Rayleigh equation analysis. The agreement confirms the accuracy of the eigenvalue analysis of the Rayleigh equation.

The maximum of the growth rate for all wavenumbers for the barotropic instability of the Gaussian jet is $\gamma \approx 0.186$. In figure 6, the growth rate for the inertial instability exceeds this value for a wide range of Ro. This is true of the finite Re cases as well

as for the inviscid limit. In the case of the inviscid limit the inertial instability is faster than the barotropic instability from $Ro \approx 1.23$ to $Ro \approx 23.6$. Recall that $Ro_{cr} \approx 1.17$ (see (2.6)). Thus, the inertial instability is faster than the barotropic from Ro close to Ro_{cr} to extremely high values of Ro, high at least in an oceanographic or atmospheric context. From the data in figure 6, we see that even for the $Re = 1250$ case, the inertial instability is faster than the inviscid barotropic instability from $Ro \approx 1.6$ to some value much above $Ro = 5$. Thus the idea of separating the effects of inertial and barotropic instabilities in predicting the full three-dimensional flow evolution is well founded.

We must also consider the possibility that the effect of the inertial instability in changing the basic jet profile may induce a barotropic instability that is faster than that of the Gaussian jet. To check whether this is the case, we calculated the growth rates for the most unstable modes of the inertial instability equilibrated jet profiles for $Ro = 2$ and $Ro = 4$ (see figure 2). We used the same method to solve the Rayleigh equation (3.3) on a discrete grid as in the case for the Gaussian jet. Let $u_0(y)$ denote the inertial instability equilibrated velocity profile that our absolute-momentum mixing construction predicts for $Ro > Ro_{cr}$. Then $u_0(y)$ replaces the Gaussian profile $U(y)$ in (3.3) for the calculation of the growth rates for $Ro > Ro_{cr}$. As in the two-dimensional numerical simulations of the equilibrated profile, we have ignored the issue of the singularities in $u_0''(y) = -\mathrm{d}\omega_z/\mathrm{d}y$ and have simply calculated u_0'' with finite differences on the grid. The resulting growth-rate curves for $Ro = 2$ and $Ro = 4$ are shown in figure 8 as long and short dashed curves, respectively. We have also tested these results from the Rayleigh equation against inviscid numerical simulations as in the Gaussian jet case. The growth rates from the simulations are shown as points in the form of open triangles and filled squares. The agreement between the simulations and the calculations based on the Rayleigh equation is very good. The result is that the peaks of both the $Ro = 2$ and $Ro = 4$ curve are $\sim 25\,\%$ lower than that for $Ro < Ro_{cr}$. For both $Ro = 2$ and $Ro = 4$, the inertially equilibrated $u_0(y)$ profile is even more stable to barotropic instability than the Gaussian profile ($Ro < Ro_{cr}$). Thus, the equilibration by inertial instability does not make the flow more barotropically unstable.

All three curves in figure 8 are peaked near $k_x = 1$, which is the mode that we used to initiate the flow in the simulations shown in figure 7. The curves for $Ro = 2$ and $Ro = 4$ are even flatter at the top than the curve for $Ro < Ro_{cr}$. The flatter the curve, the more modes we might expect to see competing for dominance if the initial condition had a randomly generated perturbation rather than being of a single wavenumber. This suggests that in the three-dimensional problem, the inertial equilibration will lead to conditions favourable for the growth of many competing barotropic modes of wavenumber near $k_x = 1$. Further, we note that the curve for $Ro = 2$ is skewed somewhat to smaller k_x and the $Ro = 4$ curve is skewed toward higher k_x with respect to the Gaussian jet case. This suggests that inertial instability will set up conditions that will favour growth of barotropic modes of lower k_x for $Ro = 2$ and for higher k_x for $Ro = 4$ compared with inertially stable flows with $Ro < Ro_{cr}$. We will see that this is the case in §§ 4 and 5.

4. Three-dimensional simulations

We have performed a series of three-dimensional numerical simulations of the incompressible Navier–Stokes equations for flow with constant Coriolis parameter f. The initial condition for each run was taken as the Gaussian jet $u(x, y, z) = U(y)$

from (2.1) plus random uncorrelated noise of r.m.s. amplitude 10^{-3} added to each component of the velocity at each point in the domain. After performing a series of low-resolution three-dimensional simulations to test how results vary with Re, Ro and numerical resolution, we decided that, given the limits of our computational resources, we would perform three high-resolution simulations with $Re = 1250$ and $Ro = 1$, 2 and 4. The dimensions of the domain were $x \in [0, 8\pi]$, $y \in [-10, 10]$ and $z \in [0, 2\pi]$ on a grid of $512 \times 360 \times 128$ points. Comparison with simulations of lower resolution, shows that these simulations are well resolved. Before making a comparison in § 5 between our predictions and these three-dimensional simulations, we shall examine the results of these simulations to see how well the effects of inertial and barotropic instability can be seen separately in the evolution of the flow.

4.1. *Simultaneous inertial and barotropic instability in three dimensions*

In figure 9, we see the evolution of the three-dimensional flow for the cases $Ro = 2$ and $Ro = 4$, as visualized through the evolution of the streamwise vorticity field ω_x. The $Ro = 1$ case is not shown since it is inertially stable and there is no strong production of ω_x.

During the early evolution (see figure 9*a,e* at $t = 50$), vortices aligned along the flow direction form at all levels within the linearly inertially unstable region. Unlike the case of pure inertial instability, these vortices are not x-independent. The early appearance of variation of the vortex tubes in the direction of the mean flow should not be confused with the effect of barotropic instability. In the case of the three-dimensional instability of a vortex, it has been found that the rib vortices, which are analogous to the streamwise vortices shown here, that develop due to inertial instability vary in the flow direction even if the initial profile of velocity does not support barotropic instability (Gallaire & Chomaz 2003; Carnevale *et al.* 2011). Such variation is inherent in some of the inertial instability modes of the three-dimensional problem. Here the problem is more complicated because the flow is both inertially and barotropically unstable at $t = 0$, and so it is not possible to completely disentangle the two instabilities. Nevertheless, the barotropic instability develops slowly while the faster inertial instability produces the rapidly growing x-dependent modes seen in figure 9(*a,e*). The fact that the inertial instability modes in three-dimensional are not x-independent, leads us to ask whether their effect on the flow will be the same as that of the pure inertial instability, that is will absolute momentum be mixed in the same way? We will return to this point in § 4.2.

By time $t = 60$ (see figure 9*b,f*), the interactions between the streamwise vortices have become strongly nonlinear. By $t = 80$ (see figure 9*c,g*), we see that the development of the barotropic instability in that the streamwise vortices begin to display large displacements in the spanwise (y) direction. In the $Ro = 2$ case, the streamwise vortices take on a clearly sinuous pattern similar to that shown in the ω_z field in the pure barotropic instability case shown in two-dimensional simulations (see figure 7*e*). The modes of the barotropic instability in the three-dimensional case become even more evident in the vertical average of ω_z, which will be examined in § 5. Although the barotropic instability mode is somewhat less evident in the $Ro = 4$ case at time $t = 80$ (figure 9*g*), we can see that the vortex structures are less symmetrically distributed about $y = 0$ than in the $Ro = 2$ case. This is similar to the situation seen in the pure two-dimensional barotropic instability simulations (see figure 7*e,i* comparing the $Ro = 2$ and $Ro = 4$ cases at early times) where the $Ro = 4$ flow is much less symmetric than the $Ro = 2$ flow.

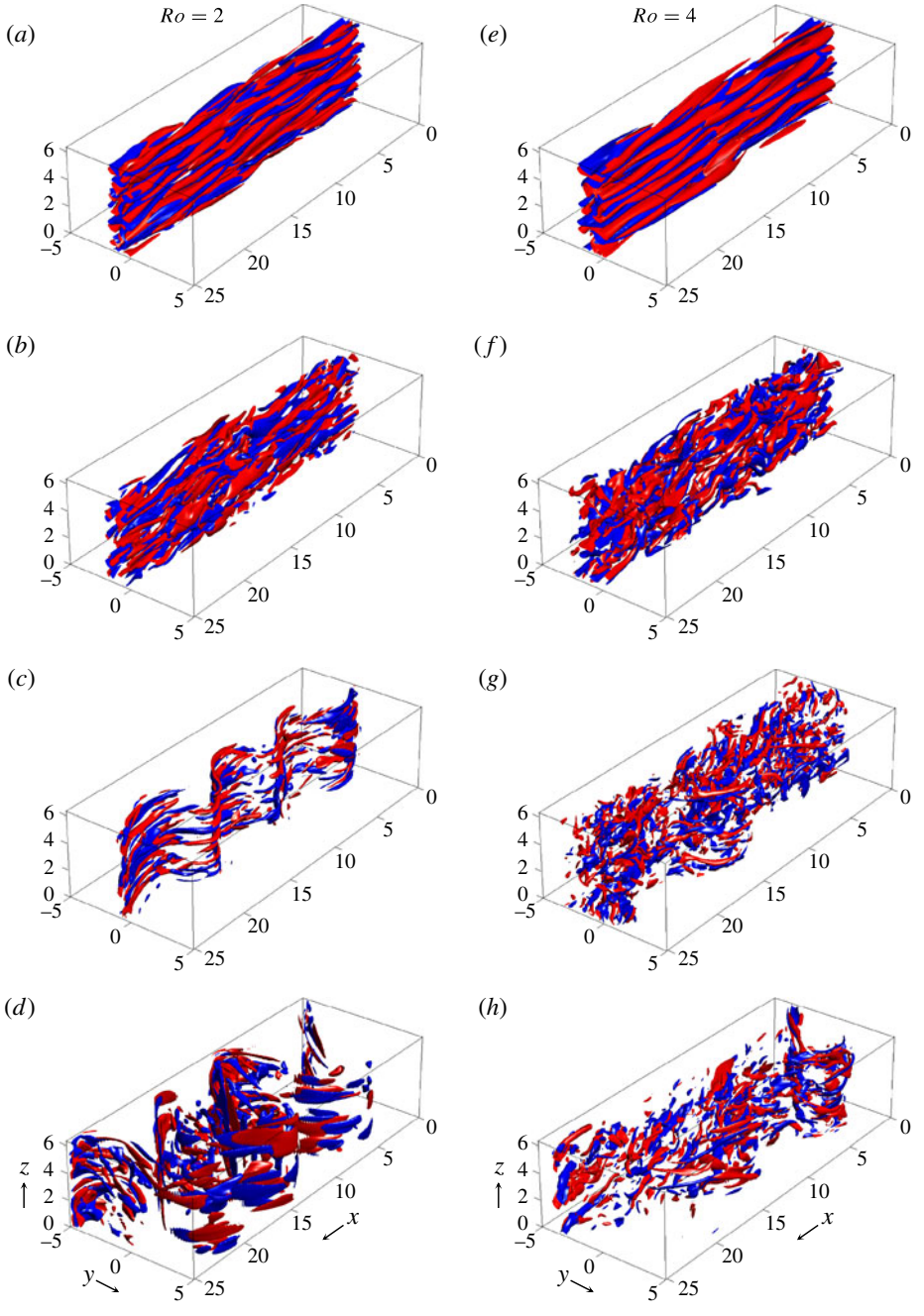

FIGURE 9. Isosurfaces of ω_x from simulations at $Re = 1250$ with $Ro = 2$ (*a–d*) and $Ro = 4$ (*e–h*), over time: (*a,e*) $t = 50$; (*b,f*) $t = 60$; (*c,g*) $t = 80$; (*d,h*) $t = 100$. Isosurface levels are $+\max|\omega_x|/6$ (red) and $-\max|\omega_x|/6$ (blue). Only the range $y \in [-5, 5]$ of the full computational range $y \in [-10, 10]$ is shown. The simulations were performed on a grid of $512 \times 360 \times 128$ points. For $Ro = 2$, (*a*) $\max|\omega_x| = 3.1$, (*b*) $\max|\omega_x| = 3.3$, (*c*) $\max|\omega_x| = 2.2$, (*d*) $\max|\omega_x| = 0.67$; for $Ro = 4$, (*e*) $\max|\omega_x| = 4.2$, (*f*) $\max|\omega_x| = 6.6$, (*g*) $\max|\omega_x| = 5.9$, (*h*) $\max|\omega_x| = 4.1$.

By $t = 100$, the barotropic instability is strongly developed and showing signs of nonlinear saturation. In fact, in § 5, we will see that by $t = 100$, the barotropic instability has resulted in the formation of coherent vortices as will be clearly seen in the vertically averaged vertical vorticity field. In figure 9(*d*) ($Ro = 2$ at $t = 100$), the streamwise vortices show clear signs of a tendency toward two-dimensionality (i.e. the variation in the z direction is becoming weaker) as one would expect from the Taylor–Proudman theorem. From the maximum magnitudes of ω_x given in the figure caption, we see that ω_x is decaying more rapidly in the $Ro = 2$ case than in the $Ro = 4$ case. From $t = 60$ to $t = 100$ the decrease is 80 % in the $Ro = 2$ case and only 40 % in the $Ro = 4$ case. The Taylor–Proudman theorem demands that these amplitudes must eventually fall to zero; however, it is reasonable that this process will be slower the higher the value of Ro (which, all else being equal, means slower ambient rotation, i.e. smaller f).

Although we do not show three-dimensional visualizations of the ω_z field, it is important to note that fluctuations in ω_z are just as strong as those in ω_x. During the evolution, values of ω_z are reached that far exceed the initial values of ω_z in the initial jet. For the Gaussian jet $\max_y \omega_z = 1/Ro_{cr} \approx 0.858$, while during the evolution of the jet with $Ro = 2$, $\max \omega_z$ reaches 2.88, with the maximum taken over the entire three-dimensional domain, and for $Ro = 4$, it reaches 6.98. By $t = 100$, these values come down to 0.899 for $Ro = 2$ and 2.76 for $Ro = 4$.

4.2. *Absolute-momentum mixing in three dimensions*

As discussed above, the streamwise vortices that arise in the early inertial instability phase as seen in figure 9(*a,e*) are different from those in the pure inertial instability in that they show significant variation in the x direction. The next question to examine is whether these x-dependent streamwise vortices mix the absolute momentum in the same way and with the same effect as do the x-independent streamwise vortices of pure inertial instability.

In figure 10, we show a cross-section of the three-dimensional flow at time $t = 50$ for: (*a*) $Ro = 2$; and (*b*) $Ro = 4$. We see that dipolar structures have formed that cause the vortices to move beyond the instability region just as in the x-independent case (see, for example, figure 4 for $Ro = 4$). In a vertical cross-section, the behaviour of the three-dimensional streamwise vortices does not seem very different from that in the x-independent case.

We next plot the profiles of the vertical and streamwise average of x-momentum $\overline{m}(y)$ and the x-velocity $\overline{u}(y)$ at several times in figure 11. For both $Ro = 2$ and $Ro = 4$, $\overline{m}$ evolves slowly at first, but then rapidly transforms to a profile that is very close to that predicted by our construction (thick solid line) based on x-independent mixing of absolute momentum. Correspondingly, $\overline{u}$ also transitions, after a slow initial phase that stays close to the Gaussian profile, very rapidly to a form close to the predicted profile. Thus, it appears that the three-dimensional modes that grow out of the inertial instability are mixing absolute linear momentum in the y direction with the same effect as achieved by the pure (x-independent) instability. This is particularly remarkable in the $Ro = 4$ case. It is amazing that the complicated tangle of streamwise vortices seen in figure 9(*e,f*) for $Ro = 4$ can produce the mean velocity field shown in figure 11(*d*) that is so close to the prediction based on x-independent flow and to the result from x-independent simulation (figure 5*b*).

In Kloosterziel *et al.* (2007*b*), through simulations of streamwise-uniform flow, we demonstrated that the match between the mean flow after inertial instability and the flow predicted by our absolute-momentum mixing construction improves with

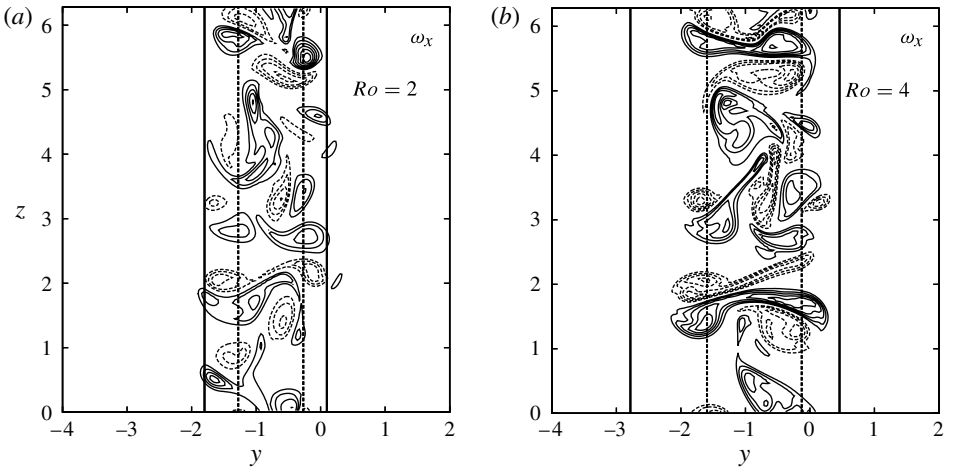

FIGURE 10. Contour plots of ω_x in a vertical cross-section of the three-dimensional flows with $Re = 1250$ at $t = 50$: (*a*) $Ro = 2$; (*b*) $Ro = 4$. Solid/dashed contours represent positive/negative ω_x with contour interval $\Delta\omega_x = 0.4$. The dashed vertical lines are the bounds of the inertial instability range given by the linear instability criterion $Q < 0$. The solid vertical lines are the bounds of the equilibration range according to our construction (see figure 2 for the $Ro = 4$ case). Only a portion of the full computational range $y \in [-10, 10]$ is shown. Similar cross-sections for pure inertial (x-independent) instability are shown in figure 4.

increasing Re. In figure 12, we show the vertical and streamwise average of absolute x momentum $\overline{m}(y)$ and x velocity $\overline{u}(y)$ for the three-dimensional evolution with two different values of Re. The variation with Re is not very strong, but it is systematic: the higher the value of Re, the closer the results are to the predicted profiles. These simulations were run with coarser resolution than in our three high-resolution simulations. Nevertheless, this resolution appears adequate for this demonstration that even in three-dimensional, the fit with the predicted inertial-instability equilibrium improves with increasing Re.

We have seen, in this section, that in the three-dimensional flow there is rapid development of x-dependent inertial modes in the early phase of the evolution ($t \lessapprox 60$). This phase of the flow results in mixing of the absolute momentum such that the effect on the vertically and streamwise-averaged absolute momentum and streamwise velocity are as predicted by our construction, just as in the x-independent flow simulation. The evolution of the vertically and streamwise-averaged absolute momentum and streamwise velocity show no significant effect of the barotropic instability in this phase of the flow. The effects of the more slowly developing barotropic instability are not significantly felt until the second phase of the flow ($t \gtrapprox 60$). The effects of barotropic instability can be seen in the strong bending of the streamwise vortices away from the x-direction in the three-dimensional isosurface plots (figure 9). The full effect of the barotropic instability will be seen more clearly in plots of the vertical average of the vertical vorticity ω_z in the next section.

5. Three-dimensional evolution versus prediction

All of the ingredients necessary to predict the outcome of the evolution of a jet in homogeneous rotating flow have been given in §§ 2 and 3. The prediction

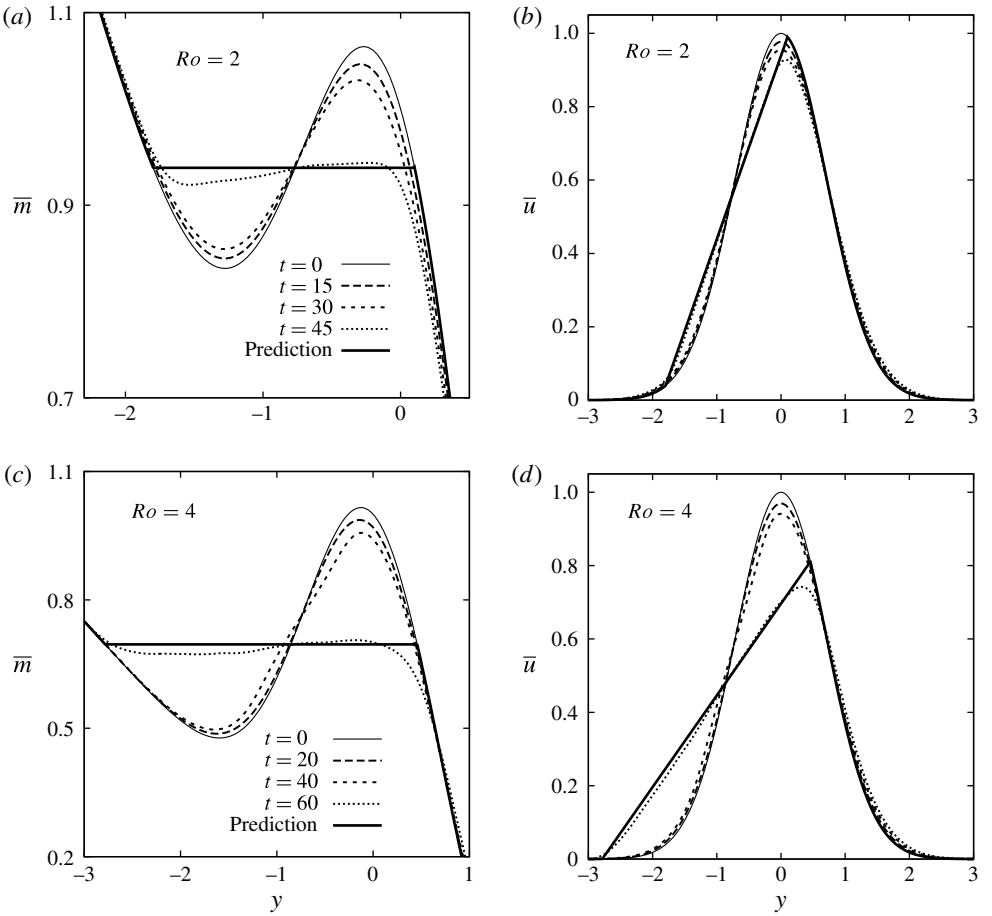

FIGURE 11. Evolution of profiles of the absolute-momentum and velocity averaged over x and z from three-dimensional simulations with $Re = 1250$ for the cases $Ro = 2$ and $Ro = 4$. (*a,c*) After an initial slow viscous evolution, the absolute momentum $m(y) = u - y/Ro$ changes rapidly to approximate our prediction based on angular momentum conservation. (*b,d*) After an initial slow viscous evolution, the velocity $u(y)$ changes rapidly to achieve the linear profile in the regime predicted by the absolute momentum construction. The curve for $t = 60$ in (*b*) is almost coincident with the prediction and may be difficult to discern. Only a portion of the full computational range $y \in [-10, 10]$ is shown.

scheme is now straightforward. It is a two-step scheme. In the first step, we use our momentum-mixing construction, as illustrated in figure 2, to provide the profile that would result due to inertial instability acting alone on a jet of a given profile and given Ro, all in the context of x-independent flow. In the second step, we use the profile obtained in step one to represent the whole effect of inertial instability on the three-dimensional evolution of the jet. The equilibrated profile, for the appropriate Ro, is used as the basis for the initial condition of a pure two-dimensional simulation that is used to capture the subsequent barotropic instability. These two-dimensional simulations are similar to those of § 3 above (see figure 7), but with a very different kind of initial perturbation. In § 3 we used a perturbation (3.1) that initially excited only a single wavenumber k_x, near the wavenumber of maximum growth. The choice

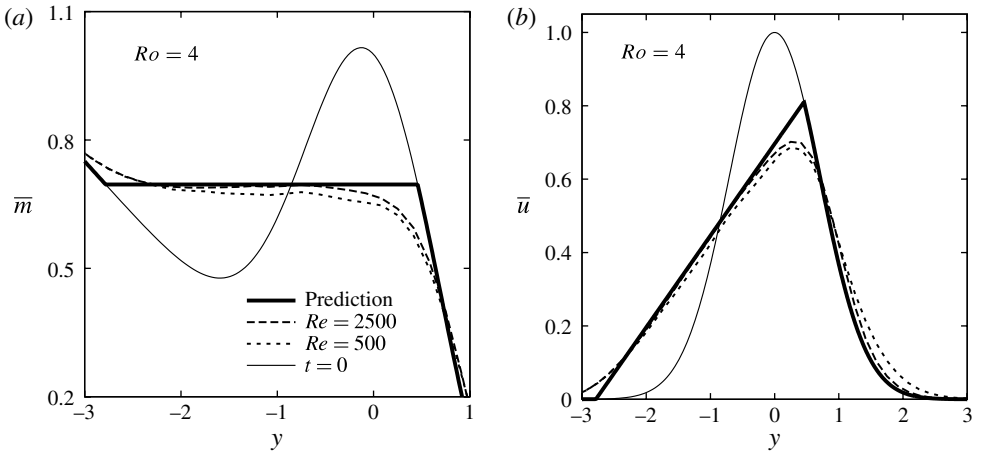

FIGURE 12. Profiles of the absolute momentum and velocity averaged over x and z at $t = 60$ from three-dimensional simulations at $Ro = 4$ with $Re = 500$ and $Re = 2500$. (a) The absolute momentum $\overline{m}(y) = \overline{u} - y/Ro$ approaches our prediction based on angular momentum conservation more closely as Re increases. (b) The higher Re, the more closely the average velocity $\overline{u}(y)$ approaches a linear profile in the regime predicted by the absolute-momentum construction. The computational domain for these simulations was $x \in [0, 8\pi]$, $y \in [-16, 16]$ and $z \in [0, 2\pi]$ on a grid of $256 \times 193 \times 65$ points.

of this wavenumber determined the number of vortices that would emerge from the evolution. Since we are now trying to predict the evolution that would evolve in a three-dimensional flow with a small-scale randomly generated initial perturbation, it is natural to add a small-scale random initial perturbation to our initial two-dimensional profile in the two-dimensional simulations in the second step of the prediction scheme. This presumably excites all possible growing barotropic modes and the dynamics of the evolution will choose the final state, just as in the three-dimensional flow.

5.1. *The need for an ensemble of two-dimensional simulations*

Predicting the three-dimensional flow is complicated by the fact that the graphs for the barotropic instability growth rate as a function of k_x, shown in figure 8 for the Gaussian jet and for the $Ro = 2, 4$ inertially equilibrated flows, are all rather broad. This means that in simulations (both two-dimensional and three-dimensional) with random initial conditions, there will be strong competition between modes with different k_x to dominate the flow. If there were no nonlinear interactions, the fastest growing mode would eventually dominate and this would be easy to predict. However, in these simulations, as the unstable modes grow nonlinear effects eventually take over creating the vortices that are observed as the current breaks up. Which mode is dominant when nonlinear effects take over depends on the amplitude of each mode initially as well as the accumulated effects of the nonlinear interactions that grow in strength during the instability. The formation of the vortices is also affected by the presence of non-vanishing viscosity. Thus, we cannot predict with certainty the number of cyclones/anticyclones that will emerge from random initial conditions. However, a statistical prediction can be made. This is done by creating an ensemble of two-dimensional simulations for each value of Ro of interest. This involves running many simulations which differ only in the seed for the random number generator that is used to create the initial random perturbation for the initial condition in step 2. We have

created ensembles for each of the three Ro that correspond to the Ro of the three high-resolution numerical simulations that we have performed, that is $Ro = 1$, 2 and 4. Note that the basic profile for the $Ro = 1$ case is just the Gaussian profile since $1 < Ro_{cr}$ and, hence, the Gaussian profile is not changed by inertial instability. For $Ro = 2$ and 4, the modified profiles predicted by our absolute-momentum-mixing construction are used. The domain for the two-dimensional simulations was chosen to have the same horizontal dimensions as in the three-dimensional simulation ($x \in [0, 8\pi]$ and $y \in [-10, 10]$) and the same resolution (512×360 gridpoints). From these ensembles of two-dimensional simulations, we accumulate statistics to predict the outcome of the three-dimensional simulations.

Our prediction scheme can be used to predict the mean number of vortices that will emerge from the three-dimensional evolution of the Gaussian jet. The number of vortices that emerge from a three-dimensional simulation depends on the value of Ro, the Reynolds number of the flow, the length of the domain, and the amplitude and seed of the randomly generated perturbations. These variables will also effect the outcome of our two-dimensional simulations in the second step of our prediction scheme, with the effect of Ro being felt through the choice of the initial basic profile. We have seen that for high values of Ro (e.g. $Ro = 4$ as illustrated in the rightmost column of figure 7) the result can be expected to have strong cyclones but anticyclones that are so weak as to be difficult to differentiate from the wide background of anticyclonic vorticity. Thus, in this discussion we will focus on predicting only the number of cyclones produced by the combined inertial and barotropic instabilities.

Given the length of the domain in these three-dimensional and two-dimensional simulations, only wavelengths $\lambda = 8\pi/n$ are possible for n some integer. Thus, only modes $k_x = 2\pi/\lambda = n/4$ may contribute to the barotropic instability. If one of these dominates at the time when nonlinear effects become significant, it should produce n cyclones. Then, however, as the flow evolves, like-signed vortices merge, through nonlinear interaction, resulting in fewer vortices (Melander, Zabusky & McWilliams 1988; Carnevale *et al.* 1991). Thus, once the vortices are formed, their number decays with time. In a finite domain, the number of vortices will continue to decrease until we are left with a single cyclone and a single anticyclone, but that is the very long-term result (Carnevale *et al.* 1991, 1992; Matthaeus *et al.* 1991; Montgomery *et al.* 1992).

In order to make a comparison with the three-dimensional simulations, we ran a series of 100 two-dimensional simulations for each $Ro(=1, 2, 4)$. Within each series, only the seed of the random number generator for the initial perturbation was varied. The r.m.s. amplitude of the initial perturbation velocity was taken to be 10^{-3}, as in the three-dimensional simulations. Also, in these two-dimensional simulations, as in the three-dimensional simulations, we set $Re = 1250$. From the two-dimensional simulations, we created a census of the maximum number of cyclones that emerge in each simulation. It is important to emphasize that the number of cyclones recorded for each simulation is the maximum number of observed cyclones because the total number of cyclones will decay in time through merger. Various methods of making this census were considered. Just counting 'by eye' the maximum number of coherent cyclones observed in the ω_z contour plots seemed adequate in most cases; however, there were some cases that were ambiguous. To make the counting systematic, after some experimentation, we decided on using the $(9/10)\max\omega_z$ contour as a guide. After the linear instability phase, this contour breaks into rings and sometimes crescent-shaped filaments. The maximum number of rings (not including the filaments) observed at any time during the run defines the number of cyclones n for that run. The results are reported in table 1 as percentages of occurrence for each n. The

Ro	$n=3$	$n=4$	$n=5$	$\langle k_x \rangle$
1	7	86	7	1
2	24	76	0	0.94
4	0	55	45	1.11

TABLE 1. Statistics for the ensembles of two-dimensional simulations used in predicting the outcome of the three-dimensional simulations. The value n is the number of cyclones that emerge from the barotropic instability. The columns under each value of n give the frequency of occurrence of that number of cyclones as a percentage. The ensemble average $\langle k_x \rangle$ is given by $\langle k_x \rangle = \langle n \rangle /4$ where $\langle n \rangle$ is the percentage weighted mean of n.

ensemble average $\langle n \rangle$ for each Ro is a percentage weighted mean. The ensemble mean wavenumber $\langle k_x \rangle$ is computed from $\langle n \rangle$. Explicitly, we have $\langle k_x \rangle = \langle n \rangle /4$ (the factor of 4 comes from the fact that the domain is $4 \times 2\pi$ long).

From table 1, we see that for $Ro = 1$, the Gaussian profile case, the dominant barotropic mode creates four cyclones, corresponding to growth of the $k_x = 1$ mode. The cases $n = 3$ and $n = 4$ are equally represented, each with 7 % of the runs. The average wavenumber for $Ro = 1$ then is $\langle k_x \rangle = 1$. For $Ro = 2$ the distribution shifts toward lower n. The $n = 3$ state then represents 24 % of the runs and there are no $n = 5$ runs. The average k_x is shifted to the lower value $\langle k_x \rangle = 0.94$. For $Ro = 4$ the distribution of the values of n has shifted toward higher values. There are in this case no instances with $n = 3$ and 45 % of the runs have $n = 5$. This gives $\langle k_x \rangle = 1.11$, the highest value of $\langle k_x \rangle$ for the three values of Ro tested.

The variation of the distribution of n with the change in Ro follows from the shift in the barotropic instability growth rates shown in figure 8. The correspondence between n and k_x in that figure is simply $k_x = n/4$. The growth-rate curve for $Ro < Ro_{cr}$ (the Gaussian jet case) is centred near $k_x = 0.9$ as discussed in § 3. The growth-rate curve is shifted in the direction of low k_x in going from $Ro = 1$ to $Ro = 2$, and toward high k_x in going from $Ro = 1$ to $Ro = 4$.

We have attempted to create a simple model to predict the mean k_x just based on competition between randomly excited growing modes with growth rates a given function of k_x. This, however, fails to predict the ensemble results for at least two reasons. One is that the process of merger of like-signed vorticity is operating during a significant period of the evolution and not just after the emergence of coherent vortices. The second is the presence of viscosity which has two effects: it changes the distribution of growth rates and it broadens vortex structures. In the final analysis it seemed that the ensemble prediction was the safest way to proceed.

5.2. *Direct comparison of three-dimensional results with predictions*

We can now turn to making a direct comparison between our three-dimensional simulations represented in figure 9 and our predictions. It would be ideal to have an ensemble of high-resolution three-dimensional simulations to compare with our two-dimensional ensembles, but due to limitations in time and computer facilities, we are limited to the three three-dimensional simulations discussed above. Given that limitation, we compare each three-dimensional simulation, with a member of the two-dimensional ensemble (of the appropriate Ro) chosen to have the same number of cyclones and a vorticity distribution reasonably close to the vertical average of the three-dimensional simulation.

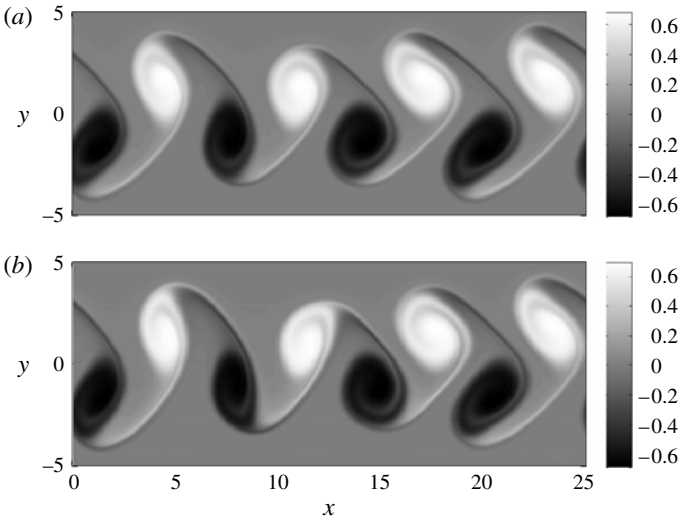

FIGURE 13. Comparison of a two-dimensional prediction of ω_z with $\overline{\omega_z}$, the vertically averaged ω_z, from a three-dimensional simulation for the case $Ro = 1$ where there is no inertial instability. (*a*) The prediction at time $\tau = 115$ is the result of a two-dimensional simulation of the Gaussian jet with a small-scale random initial perturbation. (*b*) Three-dimensional simulation result at $t = 100$. In both cases $Re = 1250$. Only a portion of the full computational range $y \in [-10, 10]$ is shown. Here the sinuous $k_x = 1$ barotropic instability mode dominates producing $n = 4$ cyclones.

5.2.1. *Case* $Ro = 1$*: inertially stable*

We start with the case $Ro = 1$. Here there is no inertial instability. The three-dimensional flow initially has an added vertical velocity perturbation, but this remains small and slowly decays. Since there is no inertial instability, the flow is always primarily barotropic, and the evolution is dominated by barotropic instability just as in two-dimensional flow. Figure 13 shows the comparison between: (*a*) ω_z in a two-dimensional simulation of the Gaussian jet; and (*b*) the vertically averaged ω_z in a three-dimensional simulation of the Gaussian jet. We denote time in the two-dimensional simulation by τ instead of t to emphasize that they are very different types of simulations, and we do not expect the time scales to match up.

In this three-dimensional simulation, the wavenumber $k_x = 1$ (four wavelengths on an 8π domain) dominates yielding four cyclones ($n = 4$). Thus, a simulation with $n = 4$ was chosen from the ensemble of two-dimensional simulations for comparison. The two-dimensional simulation captures all of the features of the vertically averaged three-dimensional flow very well. Note that the symmetry in the shapes and vorticity amplitudes of the cyclones and anticyclones is also found in the three-dimensional flow. There is nothing in the physics of the three-dimensional flow at $Ro = 1$ to break that symmetry other than the randomness of the initial conditions.

5.2.2. *Case* $Ro = 2$

A comparison between the three-dimensional flow and our prediction for $Ro = 2$ is made in figure 14. Here the jet profile used in the two-dimensional simulation is the inertial instability equilibrated flow predicted for $Re = \infty$ by our construction. The initial profile for the three-dimensional flow is just as in the three-dimensional simulation for $Ro = 1$, that is the Gaussian jet. In this three-dimensional simulation,

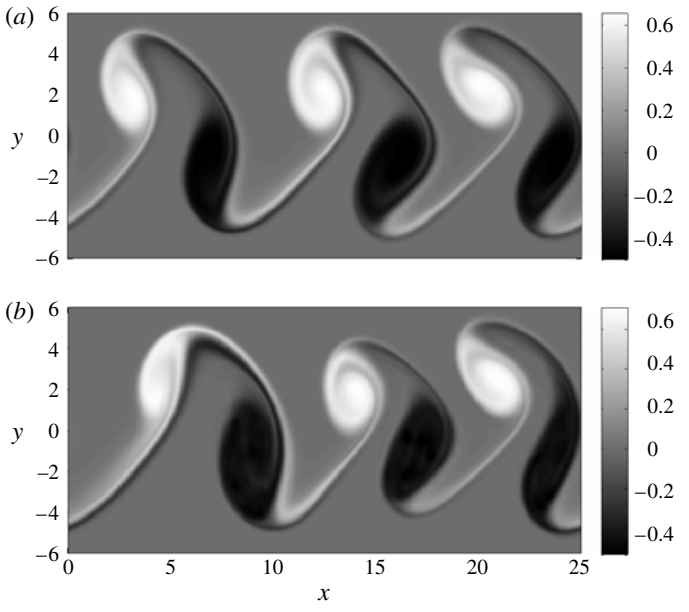

FIGURE 14. Comparison of ω_z from the prediction based on a two-dimensional simulation with $\overline{\omega_z}$, the vertically averaged ω_z, from a three-dimensional simulation for the case $Ro = 2$. (*a*) Prediction based our construction and the two-dimensional simulation result at $\tau = 125$. (*b*) Three-dimensional simulation result at $t = 100$. Comparison of three-dimensional simulations and two-dimensional predictions for $Ro = 2$. In both cases $Re = 1250$ is used. Only a portion of the full computational range $y \in [-10, 10]$ is shown. Here the sinuous $k_x = 3/4$ barotropic instability mode dominates producing $n = 3$ cyclones.

with $Ro = 2$, a $k_x = 3/4$ mode dominated, as can be seen even in the three-dimensional field of ω_x shown in figure 9(*c,d*). Thus, as discussed above, it is appropriate to compare the vertically averaged ω_z from the three-dimensional run to a two-dimensional simulation (from the $Ro = 2$ ensemble) in which the $k_x = 3/4$ mode dominates. Again the correspondence between the prediction in figure 14(*a*) and the averaged three-dimensional flow in figure 14(*b*) is very good in all aspects. In particular, note the similarity in vortex shapes and the fact that the vorticity range of the anticyclones has been reduced by the same amounts in the two-dimensional and three-dimensional cases. The asymmetry in the shape and vorticity amplitudes of the cyclones and anticyclones in the two-dimensional simulation can be directly traced to the asymmetry in the initial condition (which comes from our momentum-mixing construction for $Ro = 2$). The same asymmetry in the three-dimensional flow comes from the three-dimensional inertial instability that occurs somewhat faster than, but simultaneously with, the barotropic instability.

5.2.3. *Case* $Ro = 4$

Finally, we examine the $Ro = 4$ case. This is the most challenging case because there are strong three-dimensional motions that persist well into the barotropic instability phase of the flow as can be seen in figure 9(*g,h*). It is rotation that suppresses motion along the z-direction according to the Taylor–Proudman theorem. Hence, the higher the value of Ro the longer the three-dimensional motions tend to persist. Nevertheless, we see here that the comparison in terms of the vortex structures

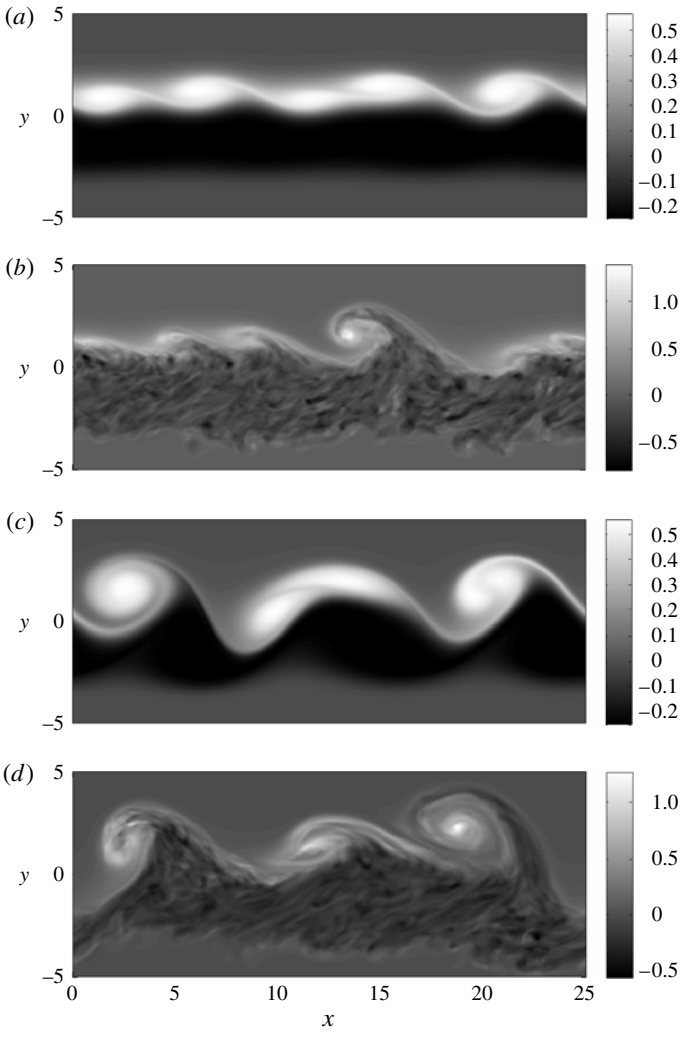

FIGURE 15. Comparison of three-dimensional simulations and two-dimensional predictions for ω_z for the case $Ro = 4$. (*a,c*) Predictions based on our construction and two-dimensional simulations at times $\tau = 118$ and $\tau = 140$. (*b,d*) Predictions of $\overline{\omega_z}$, the vertically averaged ω_z, from the three-dimensional simulation of the Gaussian jet at times $t = 80$ and $t = 100$. Only a portion of the full computational range $y \in [-10, 10]$ is shown. Here the sinuous $k_x = 5/4$ barotropic instability mode dominates producing $n = 5$ cyclones.

is remarkably good even for $Ro = 4$. In figure 15(*a,b*), we show the two-dimensional prediction and the three-dimensional vertically averaged flows at an early stage of the flow. In both panels there is a broad relatively weak anticyclonic band on the negative y side of the jet that extends slightly into the positive y side, just as expected from the construction shown in figure 2(*d*). The jet is bounded on the positive y side by a thinner, more intense layer of cyclonic vorticity that is already tending to roll up into vortices.

In figure 15(*a*), although the flow is clearly a mix of modes, with five vortices forming on the cyclonic side of the jet ($n = 5$), the flow appears to be dominated by

a $k_x = 5/4$ mode. In the three-dimensional case, figure 15(*b*), the flow also appears dominated by a $k_x = 5/4$ mode. By the later times shown in figure 15(*c,d*), for both the two-dimensional prediction and the three-dimensional vertically averaged field, mergers have occurred leaving basically a $k_x = 3/4$ mode dominant. Note that in both figure 15(*c,d*) the middle cyclonic vortex is still in an active state of merging. The nonlinear process of merger of like-signed vortices will continue in a confined domain until there is only a single cyclone and a single anticyclone left as mentioned above in the context of the two-dimensional simulations.

The important difference between our predictions based on two-dimensional simulations and the evolution of the vertically averaged ω_z of the three-dimensional simulation is the presence of the small-scale fluctuations seen in figure 15(*b,d*). In the two-dimensional case, figure 15(*a,c*), the anticyclonic band of vorticity remains as smooth as it is in the initial condition, while in the three-dimensional case, stretching and tilting of absolute vorticity in the inertial instability phase of the flow has produced lots of intense small-scale fluctuations that are very pronounced. In addition, we see that the ranges of both cyclonic and anticyclonic vorticity in the flow are different for the two-dimensional predictions and the three-dimensional flow. The extrema of the vertically averaged ω_z, in the three-dimensional flow are roughly double that in the two-dimensional prediction. In the two-dimensional simulation, due to the lack of vortex stretching and the presence of viscous diffusion, the maximum vorticity must be less than the initial value, $\max \omega_z = 1/Ro_{cr} \approx 0.858$, and the minimum value must be less negative than its initial value, $\min \omega_z = -1/Ro = -0.25$.

By examining the three-dimensional vorticity field, we find that the difference between the ranges of vorticity in the two-dimensional and three-dimensional flows is due to isolated extreme values of vorticity embedded in the three-dimensional flow. These extreme values of vorticity must level out as time proceeds since the flow must eventually become two-dimensional in accord with the Taylor–Proudman theorem. However, in terms of predicting vortex structure and the evolution of the barotropic instability, we cannot wait for complete two-dimensionalization because the phase shown here is perhaps the most interesting phase of the flow. Thus, we are forced to consider the flow before complete two-dimensionalization has occurred. Given that the circulation of vortices determine the strength of their interactions in the evolution of the barotropic instability, the mean positive and negative circulations are probably more relevant to our comparison than extreme isolated values of relative vorticity. If the vertically averaged vorticity shown in figure 15(*b,d*) is used in formula (2.10), then the result for the positive circulation per unit length is $\Gamma_+/L_x = 0.694$ at $t = 80$ and $\Gamma_+/L_x = 0.636$ at $t = 100$. These values compare well with the results for the two-dimensional flow shown in figure 15(*a,c*): $\Gamma_+/L_x = 0.666$ at $\tau = 105$ and $\Gamma_+/L_x = 0.663$ at $t = 125$.

6. Conclusion

We have explored the possibility of predicting the result of the three-dimensional instability of an initially barotropic current using the Gaussian jet as a model. We have found that for a large range of *Ro*, the inertial instability is faster than the barotropic instability (see figures 6 and 8). Based on this we have proposed and tested a method to predict the outcome of the three-dimensional instability.

Our prediction scheme has two steps. In the first step, illustrated in figure 2, the outcome of the inertial instability of the jet is predicted by using a construction based on mixing of the absolute linear momentum of the jet subject to conservation

of total momentum. It had been previously shown in Kloosterziel *et al.* (2007*b*) that this construction predicts very well the redistribution of absolute momentum in streamwise independent flow, as was demonstrated again here in figure 5. Now, we have demonstrated here that this construction predicts very well the redistribution of momentum in the fully three-dimensional evolution of the jet as shown in figure 11. It had also been previously shown that the match between our construction and mixing in streamwise-independent simulations improves with increasing Re. Here we have further demonstrated that the match between our construction and the vertically averaged three-dimensional flow also improves with increasing Re (see figure 12). It is remarkable that this construction, originally based on simulations of streamwise-independent flow (Kloosterziel *et al.* 2007*b*), does so well in capturing the effect of inertial instability in a highly three-dimensional flow. In particular, for the high-Rossby-number case that we showed, $Ro = 4$, it is impressive that the three-dimensional flow illustrated in figure 9(f), on vertical averaging, corresponds so well to our construction (see figure 11d).

In the second step of our prediction scheme, the inviscid predictions of our momentum-mixing construction are used as the initial conditions for two-dimensional simulations. An ensemble of such two-dimensional simulations was used to predict the statistics of the full three-dimensional flow. Table 1 gives the ensemble predictions for how the number of vortices produced by the combined centrifugal and barotropic instabilities should vary with Ro. An average over the ensemble results (see $\langle k_x \rangle = \langle n \rangle / 4$ in table 1) leads to the prediction that, with respect to the inertially stable case $Ro = 1$, the mean number of cyclones $\langle n \rangle$ should be higher for $Ro = 4$ and lower for $Ro = 2$. This prediction is nicely reflected in the three three-dimensional simulations that we performed which produced four vortices at $Ro = 1$, three at $Ro = 2$ and five at $Ro = 4$.

We have also shown that the details of the vertical average of the flows from the three three-dimensional simulations compare very well with particular members of the two-dimensional ensembles, chosen to agree in Ro and n. For moderately high Ro (e.g. $Ro = 2$), we were able to predict quite accurately the shape and vorticity amplitudes of the vortices that emerge from the full three-dimensional instability. One of the key differences between the evolution of the inertially stable jet (e.g. at $Ro = 1$) and the inertially unstable jet ($Ro > Ro_{cr} \approx 1.17$) is that the anticyclonic vorticity amplitude in the final vortices can be much smaller than that in the cyclonic vortices in the inertially unstable case. We were able to correctly predict this difference quantitatively in the $Ro = 2$ case. Qualitatively the same effect was reproduced in the $Ro = 4$ case, although quantitatively the peak magnitudes of both cyclonic and anticyclonic vorticity were larger than anticipated in that case. We argued that the differences in extreme values in the vertically averaged three-dimensional vorticity field could be traced to isolated extrema of vorticity in the three-dimensional field. Furthermore, we suggested that these extrema may not play a significant role in the barotropic instability that determines the number of vortices that are born from the evolution of the jet. This is verified by the fact that the net positive and negative circulations in the three-dimensional flows are well predicted by the two-dimensional flows and the fact that the vertically averaged ω_z field matches the two-dimensional predictions well except for small-scale fluctuations.

A natural extension of the work presented here would be to take into account the effect of a stable density stratification in the vertical direction. In the problem of inertial instability of a vortex with its axis aligned along the axis of ambient rotation, Kloosterziel *et al.* (2007*a*) found that, for $Re \to \infty$, the effect of mixing

angular momentum could be predicted by a construction similar to that used here for mixing absolute linear momentum. In the vortex problem, the vortices that arise due to inertial instability are aligned in the azimuthal direction, that is along the basic flow direction, and are sometimes called rib vortices. In the case with stratification, if the ambient rotation axis, the axis of the vortex and the vertical direction all coincide, then the thickness of these rib vortices in the vertical direction is strongly affected by stratification. The stronger the stratification of the flow, the flatter are rib vortices. However, with increasing Re, for any degree of stratification, the trend is toward the same equilibrium state predicted by our angular momentum mixing construction for the unstratified case (Kloosterziel *et al.* 2007*a*). The situation should be the same if stratification is added to the planar shear flows studied in Kloosterziel *et al.* (2007*b*) and we expect that stratification will not affect the final equilibrium state by much in the limit $Re \to \infty$.

One effect that the presence of stratification adds is the possibility to lose energy to internal wave radiation. For the vortex, this loss is minor being less than 1 % of the total energy loss during equilibration. We may expect similar results for an x-independent simulation of the jet in stratified flow. On the other hand, in stratified simulations of a horizontal shear constrained to be independent of variation in the flow direction, Plougonven & Zeitlin (2009) found that in addition to the barotropic component of the flow, which is well predicted by our construction, there is a residual baroclinic component that involves strong density gradients at small scales, and these only disappear slowly through diffusion. In addition, Plougonven & Zeitlin (2009) found that there are subinertial waves that become trapped in the region of strong anticyclonic vorticity. These effects may complicate the analysis of the evolution of the jet in stratified three-dimensional flow.

Finally, we note that physical mechanisms other than inertial instability can break the symmetry between cyclones and anticyclones in the evolution of an initially symmetric jet. For example, Poulin & Flierl (2003) examined the barotropic instability of a Gaussian jet in a shallow-water model with a free surface. They show that, depending on the values of the Rossby and Froude (Fr) numbers, the vorticity amplitudes may be found to be higher in either the cyclones or the anticyclones. In particular, for high Ro and small Fr, they find a pattern similar to our figure 7(*j*); however, in their case, the anticyclonic vorticity dominates and it is the cyclonic vorticity that develops the triangular shape. Such patterns may be expected to form whenever one sign of vorticity is suppressed relative to the other by whatever mechanism breaks the symmetry.

Acknowledgements

G.F.C. acknowledges support from National Science Foundation grant OCE 11-29059. R.C.K. acknowledges support from National Science Foundation grant OCE 10-32256. We thank San Nguyen for his help with Matlab.

Appendix. Inertial instability eigenvalue problem

We begin by linearizing the Navier–Stokes equations about the basic state with $u = U(y)$ and $v = w = 0$. We assume further that no variation is allowed in the x direction. The result, written in dimensional form, is (see, for example, Kloosterziel & Carnevale 2008)

$$\mathrm{D}_v u' - Q v' = 0 \qquad \text{(A 1}a\text{)}$$

$$\mathrm{D}_\nu v' + fu' = -\rho_0^{-1}\partial_y p' \tag{A 1b}$$

$$\mathrm{D}_\nu w' = -\rho_0^{-1}\partial_z p' \tag{A 1c}$$

$$\partial_y v' + \partial_z w' = 0 \tag{A 1d}$$

where the primed variables are the perturbation variables (u, v, w the velocity components, p pressure and ρ_0 the constant density), $Q = f - \mathrm{d}U/\mathrm{d}y$ and $\mathrm{D}_\nu = \partial_t - \nu(\partial_y^2 + \partial_z^2)$.

Cross-differentiating and subtracting the second and third equations in (A 1) yields

$$\mathrm{D}_\nu u' - Qv' = 0, \tag{A 2a}$$

$$\mathrm{D}_\nu(\partial_y w' - \partial_z v') - f\partial_z u' = 0. \tag{A 2b}$$

The incompressibility condition (last line of (A 1)) allows us to write $v' = -\partial_z\psi$ and $w' = \partial_y\psi$ with ψ the streamfunction for the meridional motions. Thus, we have

$$\mathrm{D}_\nu u' + Q\partial_z\psi = 0 \tag{A 3a}$$

$$\mathrm{D}_\nu(\partial_y^2 + \partial_z^2)\psi - f\partial_z u' = 0. \tag{A 3b}$$

Normal modes for this problem take the form: $[u', \psi] = \mathrm{Re}\{[\tilde{u}(y), \tilde{\psi}(y)]\mathrm{e}^{st+\mathrm{i}k_z z}\}$. Thus, for normal modes (A 3) becomes

$$(s - \nu(\partial_y^2 - k_z^2))\tilde{u} + \mathrm{i}k_z Q\tilde{\psi} = 0 \tag{A 4a}$$

$$(s - \nu(\partial_y^2 - k_z^2))(\partial_y^2 - k_z^2)\tilde{\psi} - \mathrm{i}k_z f\tilde{u} = 0. \tag{A 4b}$$

In order to achieve the normal eigenvalue equation form, we operate on the second line of (A 4) with $(\partial_y^2 - k_z^2)^{-1}$. Thus, we obtain

$$(s - \nu(\partial_y^2 - k_z^2))\tilde{u} + \mathrm{i}k_z Q\tilde{\psi} = 0 \tag{A 5a}$$

$$(s - \nu(\partial_y^2 - k_z^2))\tilde{\psi} - \mathrm{i}k_z f\,(\partial_y^2 - k_z^2)^{-1}\,\tilde{u} = 0. \tag{A 5b}$$

With a simple rearrangement of terms this can be put into the standard eigenvalue form:

$$s\phi = A\phi \tag{A 6}$$

where ϕ is the vector $(\tilde{u}, \tilde{\psi})^{\mathrm{T}}$ ('T' indicating the transpose) and $\boldsymbol{A}$ is the matrix

$$\boldsymbol{A} = \begin{bmatrix} \nu(\partial_y^2 - k_z^2) & -\mathrm{i}k_z Q \\ \mathrm{i}k_z f\,(\partial_y^2 - k_z^2)^{-1} & \nu(\partial_y^2 - k_z^2) \end{bmatrix}. \tag{A 7}$$

We can rewrite ϕ and the independent variables in non-dimensional form. Thus, in non-dimensional form the problem reduces to finding the eigenvalues of

$$\boldsymbol{A} = \begin{bmatrix} Re^{-1}(\partial_y^2 - k_z^2) & -\mathrm{i}k_z Q \\ \mathrm{i}k_z Ro^{-1}\,(\partial_y^2 - k_z^2)^{-1} & Re^{-1}(\partial_y^2 - k_z^2) \end{bmatrix}. \tag{A 8}$$

Solving the eigenvalue problem first involves discretizing y and writing the second derivative ∂_y^2 as a matrix. This was done with N gridpoints for $y \in [-L_y, L_y]$ with free slip boundary conditions assumed. Then the eigenvalues of A, a matrix of dimensions $2N \times 2N$, are conveniently determined with some efficient eigenvalue solver (in this case we used eig(A) in Matlab). A sequence of values of k_z is chosen to determine

which one, to some desired accuracy, produces the highest value of the real part of s, Re(s), i.e. the highest growth rate γ_{max} for given values of Ro and Re. We compared the results that we obtained for various values of N and various L_y. The results do not vary significantly for $L_y > 5$. The results shown in figure 6 were calculated with $L_y = 10$, which is the same value that was used in the numerical simulations that are also represented in that figure. For $L_y = 10$, variation of N showed that the values of γ_{max} converged for $N \geqslant 200$ with accuracy better than three significant figures. The results presented in figure 6 were calculated with $N = 513$.

REFERENCES

BILLANT, P. & GALLAIRE, F. 2005 Generalized Rayleigh criterion for non-axisymmetric centrifugal instabilities. *J. Fluid Mech.* **542**, 365–379.

BOUCHUT, F., RIBSTEIN, B. & ZEITLIN, V. 2011 Inertial, barotropic, and baroclinic instabilities of the bickley jet in two-layer rotating shallow water model. *Phys. Fluids* **23**, 126601.

CARNEVALE, G. F., KLOOSTERZIEL, R. C., ORLANDI, P. & VAN SOMMEREN, D. D. J. A. 2011 Predicting the aftermath of vortex breakup in rotating flow. *J. Fluid Mech.* **669**, 90–119.

CARNEVALE, G. F., MCWILLIAMS, J. C., POMEAU, Y., WEISS, J. B. & YOUNG, W. R. 1991 Evolution of vortex statistics in two-dimensional turbulence. *Phys. Rev. Lett.* **66**, 2735–2737.

CARNEVALE, G. F., MCWILLIAMS, J. C., POMEAU, Y., WEISS, J. B. & YOUNG, W. R. 1992 Rates, pathways, and end states of nonlinear evolution in decaying two-dimensional turbulence: scaling theory versus selective decay. *Phys. Fluids* A **4**, 1314–1316.

CHARNEY, J. G. 1973 Lecture notes on planetary fluid dynamics. In *Dynamic Meteorology* (ed. P. Morel). pp. 97–351. Kluwer.

DRAZIN, P. G. & REID, W. H. 1981 *Hydrodynamic Stability*. Cambridge University Press.

ELDEVIK, T. & DYSTHE, K. B. 2002 Spiral eddies. *J. Phys. Oceanogr.* **32**, 851–869.

FLIERL, G. R., MALANOTTE-RIZZOLI, P. & ZABUSKY, N. J. 1987 Nonlinear waves and coherent vortex structures in barotropic β-plane jets. *J. Phys. Oceanogr.* **17**, 1408–1438.

GALLAIRE, F. & CHOMAZ, J. M. 2003 Three-dimensional instability of isolated vortices. *Phys. Fluids* **15** (8), 2113–2126.

GRIFFITHS, S. D. 2008 The limiting form of inertial instability in geophysical flows. *J. Fluid Mech.* **605**, 115–143.

HOLTON, J. R. 1979 *An Introduction to Dynamic Meteorology*. Academic.

KLOOSTERZIEL, R. C. & CARNEVALE, G. F. 2008 Vertical scale selection in inertial instability. *J. Fluid Mech.* **594**, 249–269.

KLOOSTERZIEL, R. C., CARNEVALE, G. F. & ORLANDI, P. 2007*a* Inertial instability in rotating and stratified fluids: barotropic vortices. *J. Fluid Mech.* **583**, 379–412.

KLOOSTERZIEL, R. C. & VAN HEIJST, G. J. F. 1991 An experimental study of unstable barotropic vortices in a rotating fluid. *J. Fluid Mech.* **223**, 1–24.

KLOOSTERZIEL, R. C., ORLANDI, P. & CARNEVALE, G. F. 2007*b* Saturation of inertial instability in rotating planar shear flows. *J. Fluid Mech.* **583**, 413–422.

MARKOWSKI, P. & RICHARDSON, Y. 2010 *Mesoscale Meteorology in Midlatitudes*. Wiley-Blackwell.

MATTHAEUS, W. H., STRIBLING, W. T., MARTINEZ, D., OUGHTON, S. & MONTGOMERY, D. 1991 Decaying two-dimensional turbulence at very long times. *Physica* D **51**, 531–538.

MELANDER, M. V., ZABUSKY, N. J. & MCWILLIAMS, J. C. 1988 Symmetric vortex merger in two dimensions: causes and conditions. *J. Fluid Mech.* **195**, 303–340.

MONTGOMERY, D., MATTHAEUS, W. H., STRIBLING, W. T., MARTINEZ, D. & OUGHTON, S. 1992 Relaxation in two dimensions and the 'sinh-poisson' equation. *Phys. Fluids* A **4**, 3–6.

MUNK, W., ARMI, L., FISCHER, K. & ZACHARIASEN, F. 2000 Spirals on the sea. *Proc. R. Soc. Lond.* **456**, 1217–1280.

ORLANDI, P. & CARNEVALE, G. F. 1999 Evolution of isolated vortices in a rotating fluid of finite depth. *J. Fluid Mech.* **381**, 239–269.

PLOUGONVEN, R. & ZEITLIN, V. 2009 Nonlinear development of inertial instability in a barotropic shear. *Phys. Fluids* **21**, 106601.

POULIN, F. J. & FLIERL, G. R. 2003 The nonlinear evolution of barotropically unstable jets. *J. Phys. Oceanogr.* **33**, 2173–2192.

RIBSTEIN, B., PLOUGONVEN, R. & ZEITLIN, V. 2013 Inertial vs baroclinic instability of the bickley jet in continuously stratified rotating fluid, *J. Fluid Mech.* (submitted).

SHEN, C. Y. & EVANS, T. E. 1998 Inertial instability of large Rossby number horizontal shear flows in a thin homogeneous layer. *Dyn. Atmos. Oceans* **26**, 185–208.

SHEN, C. Y. & EVANS, T. E. 2002 Inertial instability and sea spirals. *Geophys. Res. Lett.* **29**, 1–19.

SMYTH, W. D. & MCWILLIAMS, J. C. 1998 Instability of an axisymmetric vortex in a stably stratified, rotating environment. *Theor. Comput. Fluid Dyn.* **11**, 305–322.

WINTER, TH. & SCHMITZ, G. 1998 On divergent barotropic and inertial instability in zonal-mean flow profiles. *J. Atmos. Sci.* **98**, 758–776.